Assimilating ASCAT normalized backscatter and slope into the land surface model ISBA-A-gs using a Deep Neural Network as the observation operator: Case studies at ISMN stations in western Europe

Xu Shan, Susan Steele-Dunne, Sebastian Hahn, Wolfgang Wagner, Bertrand Bonan, Clement Albergel, Jean-Christophe Calvet, Ou Ku

Remote Sensing of Environment 308 (2024) 114167

Contents lists available at ScienceDirect

Remote Sensing of Environment

journal homepage: www.elsevier.com/locate/rse

Assimilating ASCAT normalized backscatter and slope into the land surface model ISBA-A-gs using a Deep Neural Network as the observation operator: Case studies at ISMN stations in western Europe

Xu Shan [a,b,*], Susan Steele-Dunne [a], Sebastian Hahn [c], Wolfgang Wagner [c], Bertrand Bonan [d], Clement Albergel [d], Jean-Christophe Calvet [d], Ou Ku [e]

[a] Department of Geoscience and Remote Sensing, Faculty of Civil Engineering and Geosciences, TU Delft, Delft, the Netherlands
[b] Department of Water Management, Faculty of Civil Engineering and Geosciences, TU Delft, Delft, the Netherlands
[c] Department of Geodesy and Geoinformation (GEO), Vienna University of Technology, Vienna, Austria
[d] CNRM, Université de Toulouse, Météo-France, CNRS, Toulouse, France
[e] Netherlands eScience Center, Amsterdam, the Netherlands

ARTICLE INFO

Editor: Jing M. Chen

Original content: Dataset of ISBA open loop states and ASCAT normalized backscatter and slope data of grid points (Original data)

Keywords:
ASCAT
Radar
Vegetation
Data assimilation
Land surface model
Machine learning
Soil moisture

ABSTRACT

ASCAT normalized backscatter (σ^o_{40}) and slope (σ') contain valuable information about soil moisture and vegetation. While σ^o_{40} has been assimilated to constrain soil moisture, sometimes together with Leaf Area Index (LAI), this study is the first to assimilate σ' directly to constrain vegetation states. Here, we assimilate σ^o_{40} and slope σ' into the ISBA-A-gs LSM using the Simplified Extended Kalman Filter (SEKF) using a Deep Neural Network (DNN) as the observation operator. The performances of the data assimilation (DA) and open loop (OL) are evaluated against in-situ soil moisture observations from the International Soil Moisture Network (ISMN), and LAI observations from the Copernicus Global Land Service (CGLS). Given an accurate and physically plausible observation operator, along with well-defined model and observation errors, the data assimilation system should yield improved estimates of the model states. However, results show that the DA performance is neutral compared to the OL in terms of the median unbiased root mean square error (ubRMSE) and Pearson correlation coefficient (ρ) across all validation sites. In addition, an analysis of the residuals and innovations confirms that DA had limited or no impact. This poor performance is perplexing. Furthermore, given the growing interest in the use of machine-learning-based observation operators, it is essential to understand the role that the use of the DNN may be playing in this poor performance. While representativeness errors and error specification play some part, it is demonstrated that the key factor constraining the efficacy of the SEKF is the correct estimation of the Jacobians that control the degree to which the observations update the states in the SEKF. It is argued that the DNN relating model states to satellite observations must have physically-plausible and robust Jacobians for the DNN to be effective in a data assimilation framework.

1. Introduction

Land atmosphere interactions initiated by soil moisture and modulated by vegetation have a large impact on near-surface atmospheric circulation (Miralles et al., 2014; Koster et al., 2016). Thus land surface models play a crucial role in Earth system modeling and the prediction of climate extremes such as drought and heat waves (Berg et al., 2016). To improve the estimation of land surface variables (LSV) related to soil moisture and vegetation, there has been an increasing number of studies about assimilating remote sensing observations into land surface models (LSMs) (Mecklenburg et al., 2016; Lievens et al., 2017a; Bonan et al., 2020). Generally, land surface assimilation systems constrain the model with one of two types of data: a) data products retrieved from satellites, such as surface soil moisture (SSM) retrieved from satellites like the Advanced Microwave Scanning Radiometer for Earth observation science (AMSR-E) (Imaoka et al., 2010; Njoku et al., 2003; Reichle et al., 2007; Draper et al., 2009, 2012), the Soil Moisture Ocean Salinity (SMOS) mission (Kerr et al., 2010; Ridler et al., 2014; Lievens et al.,

* Corresponding author at: Department of Geoscience and Remote Sensing, Faculty of Civil Engineering and Geosciences, TU Delft, Delft, the Netherlands.
E-mail address: x.shan-2@tudelft.nl (X. Shan).

https://doi.org/10.1016/j.rse.2024.114167
Received 17 July 2023; Received in revised form 29 March 2024; Accepted 21 April 2024
Available online 2 May 2024

2015; Martens et al., 2016) and Soil Moisture Active Passive (SMAP) mission (Entekhabi et al., 2010; Mladenova et al., 2020; Pinnington et al., 2021; Seo et al., 2021), as well as leaf area index (LAI) from Copernicus Global Land Service (CGLS) (Albergel et al., 2017; Bonan et al., 2020) or station based observations (Sabater et al., 2008; Albergel et al., 2010); and b) signals directly observed by satellites such as radar backscatter (σ) observed by Advanced SCATterometer (ASCAT) (Wagner et al., 1999b; Lievens et al., 2017a; Baguis et al., 2022) and Sentinel-1 (Lievens et al., 2017b; Rains et al., 2022; Modanesi et al., 2022) or passive temperature brightness (*Tb*) from SMOS (Lannoy and Reichle, 2016a, 2016b) or SMAP (Reichle et al., 2017a; Lievens et al., 2017b; Reichle et al., 2017b; Lu et al., 2020).

Several studies demonstrated the capability of ASCAT observations to accurately capture the temporal dynamics of in-situ and modeled soil moisture observations across Europe (Albergel et al., 2009; Brocca et al., 2010). Operational soil moisture products based on ASCAT data have been available at a global scale since December 2008 (Bartalis et al., 2007), providing data with coarse spatial resolution (25/50 km) and nearly daily temporal resolution. One of the key advantages of ASCAT is the unique observation geometry, which enables measurements of the Earth's surface from different incidence angles. The dependence of ASCAT backscatter on incidence angle is closely related to the surface dielectric properties and structure, i.e. the soil moisture and vegetation water content/biomass. ASCAT provides valuable information about vegetation water dynamics via normalized backscatter (σ^o_{40}), slope ($\sigma^{'}$) and curvature ($\sigma^{''}$) derived from the Taylor expansions of backscatter to incidence angle (Hahn et al., 2017; Steele-Dunne et al., 2019; Shan et al., 2022). Diurnal differences of radar backscatter were shown to reflect the variations in vegetation water content (Steele-Dunne et al., 2012). The slope has been demonstrated to be correlated with vegetation density (Steele-Dunne et al., 2019), plant physiological conditions (Pfeil et al., 2020), plant phenology and water status (Petchiappan et al., 2021), and deep soil water availability (Shan et al., 2022).

Many studies have assimilated ASCAT surface soil moisture products into LSMs to improve the estimates of surface soil moisture, root zone soil moisture and other hydrological variables (Brocca et al., 2010; Draper et al., 2011; Albergel et al., 2012; Aires et al., 2021; Seo et al., 2021). Additionally, ASCAT products were also jointly assimilated with LAI observations into LSMs to improve the estimates of vegetation biomass (Barbu et al., 2011, 2014; Albergel et al., 2017, 2018). However, no studies concentrate on directly assimilating ASCAT normalized backscatter and slope.

Directly assimilating the microwave observations, such as σ and *Tb*, to constrain the states of LSMs (Reichle et al., 2002b; Crow and Wood, 2003; Balsamo et al., 2006; Han et al., 2014; Lievens et al., 2017a) obviates the need for cumulative density function (CDF)-matching and bias correction (Fairbairn et al., 2017; Leroux et al., 2018) and also avoids potential cross-correlated errors between retrievals and model simulations (Lannoy and Reichle, 2016a; Lievens et al., 2017a). Radiative transfer models (RTM) are commonly used as the observation operator to connect states with microwave observations. Lievens et al. (2017a) compared the assimilation of ASCAT σ^o and SMOS *Tb* into the Global Land Evaporation Amsterdam Model (GLEAM). They calibrated the Water Cloud Model (WCM, Attema and Ulaby (1978)) and L-band Microwave Emission from the Biosphere radiative transfer model (L-MEB, Wigneron et al. (2007)) to forward model ASCAT σ^o and SMOS *Tb*. The study demonstrated that assimilating ASCAT σ^o improves the model skills in surface soil moisture and land evaporation estimates. In passive microwave remote sensing, Lannoy and Reichle (2016a, 2016b) assimilated SMOS *Tb* into the GEOS-5 Catchment Catchment Land Surface Model with the $\tau - \omega$ model serving as the observation operator. The DA of SMOS *Tb* was compared to the DA of SMOS retrieval products. The assimilation of Tb showed larger innovations and local differences in performance, which were attributed to differences in how the Tb and SM observations were masked and to the different assumptions made in the retrieval model versus the forward model. A similar DA system is used for the SMAP Level 4 soil moisture product (Reichle et al., 2017b, 2021). The diagnosis of the DA system was fully examined on a global scale to assess the impact of assimilating SMAP *Tb*. In the snow assimilation community, Forman and Reichle (2015); Xue and Forman (2015) trained a machine learning model to extract information from microwave observables to constrain the LSM. Then AMSR-E *Tb* was assimilated into the Catchment model to improve the estimation of snow states.

There are few studies directly assimilating ASCAT observables into LSMs. The WCM was used as the observation operator to reconcile the information in ASCAT normalized backscatter with the states in LSM Global Land Evaporation Amsterdam Model (GLEAM) by Lievens et al. (2017a) and a hydrological model SCHEME Baguis et al. (2022). Shan et al. (2022) proposed to train a Deep Neural Network (DNN) as the observation operator for ASCAT normalized backscatter and slope. The machine-learning based observation operator directly links land surface variables to the ASCAT observables. It is not a simple emulation of an RTM because an RTM requires parameters (e.g. surface roughness, vegetation structure, vegetation water content) which are not simulated by the ISBA. The data-driven method is able to connect the states which can be modeled by ISBA to those that are observed with ASCAT. Therefore it enables assimilation of the ASCAT observables without explicitly modeling the VWC. The normalized sensitivity coefficient (NSC) was examined to ensure the physical plausibility of the model. Corchia et al. (2023) also assimilated ASCAT normalized backscatter into ISBA by using a neural network as the observation operator. Their observation operator is trained on surface soil moisture and surface soil temperature from ISBA, and LAI observations from the PROBA-V satellite. Their results show an overall improvement compared to the open-loop simulation, evaluated against PROBA-V LAI observations and in-situ soil moisture observations.

The current study is the first to explore the joint assimilation of ASCAT normalized backscatter and slope. The premise of joint assimilation of ASCAT normalized backscatter and slope is to simutaneously constrain the soil and vegetation dynamics in the LSM. Previous work achieved this by assimilating retrieved surface soil moisture products and LAI products (Sabater et al., 2007; Barbu et al., 2011, 2014; Albergel et al., 2017, 2018, 2019, 2020). They showed that assimilating the vegetation products together with soil moisture observations improves the estimate of land surface variables like evapotranspiration, SSM, LAI and CO2 fluxes (Sabater et al., 2007; Barbu et al., 2011, 2014), hydrological variables (Fairbairn et al., 2017), and other variables (Albergel et al., 2019). This can lead to improved ability to monitor and forecast drought (Barbu et al., 2014; Albergel et al., 2018), and constrain the phenological cycle in the land surface model (Barbu et al., 2011). Analogous to VOD, dynamics in ASCAT slope have been shown to reflect changes in biomass (Steele-Dunne et al., 2019), phenology (Pfeil et al., 2020) and water status (Shan et al., 2022; Petchiappan et al., 2021). One advantage of using ASCAT slope rather than VOD is that it is directly calculated from observations, thereby eliminating the need for assumptions or ancillary data. Several studies have demonstrated the assimilation of VOD along with SSM and other observations (Mucia et al., 2022; Kumar et al., 2020) improves the estimation of various land surface variables such as evapotranspiration (Kumar et al., 2020), soil moisture and GPP (Mucia et al., 2022). Thus, joint assimilation ASCAT normalized backscatter and slope should be expected to improve estimation of land surface (soil and vegetation) states.

This study builds on Shan et al. (2022) by integrating the DNN into the Météo-France's modeling platform SURFEX/LDAS Monde data assimilation framework (Albergel et al., 2017). Following the SURFEX assimilation methodology, ASCAT observables are directly assimilated into the LSM ISBA, using the observation operator developed by Shan et al. (2022). This study is conducted in western Europe using ASCAT data from 2017 to 2019, at ASCAT grid points (GPIs) containing International Soil Moisture Network (ISMN) stations. Our hypothesis is that

the joint assimilation of normalized backscatter and slope will improve surface and root zone soil moisture as well as vegetation states such as LAI, if a) the Jacobians of the observation operator is physically plausible; b) the model and observation uncertainties are reasonable and fit for the data assimilation system. The parameter settings and implementation follow previous SURFEX/LDAS Monde studies such as Albergel et al. (2017), Barbu et al. (2014) and Barbu et al. (2011). Following the approach of Reichle et al. (2017b), Kolassa et al. (2017) and Daley (1992), diagnostics based on innovations and residuals are used to assess whether the DA system is optimal and the model and observation errors are well-specified. The DA performance is evaluated against in-situ observations of soil moisture and independent LAI data from remote sensing. The DA results are compared to the LSM open loop (OL) to test the hypothesis that joint assimilation leads to improved skill.

2. Data and methodology

2.1. Data

2.1.1. ASCAT normalized backscatter and slope

ASCAT normalized backscatter and slope come from a second order polynomial which describes the ASCAT backscatter dependence on the incidence angle:

$$\sigma^o(\theta) = \sigma^o(\theta_r) + \acute{\sigma}(\theta_r)(\theta-\theta_r) + \frac{1}{2}\acute{\sigma}'(\theta_r)(\theta-\theta_r)^2, \qquad [\mathrm{dB}] \tag{1}$$

where the zeroth order term $\sigma^o(\theta_r)$ is the normalized backscatter at a reference angle (40°), and the 1st and 2nd order coefficient $\acute{\sigma}(\theta_r)$ and $\acute{\sigma}'(\theta_r)$ are so-called slope and curvature (Hahn et al., 2017). Given the values of slope and curvature, measured backscatter at any incidence angle can be extrapolated to the reference angle by:

$$\sigma^o(\theta_r) = \sigma^o(\theta) - \acute{\sigma}(\theta_r)(\theta-\theta_r) - \frac{1}{2}\acute{\sigma}'(\theta_r)(\theta-\theta_r)^2 \tag{2}$$

Each ASCAT instrument has two sets of three side-looking antennas (oriented at 45° (fore), 90° (mid) and 135° (aft) to the satellite track) each illuminating a 550 km wide swath on either side of the satellite track. Together, these provide so-called backscatter triplets [σ_f, σ_{mid}, σ_a] (Fore, Mid and Aft beam) at the incidence angles [θ_f, θ_{mid}, θ_a] (same angle 34–65° for Fore and Aft beam, 25–55° for Mid beam). Thus two local slope estimates are produced as:

$$\acute{\sigma}\left(\frac{\theta_{mid}-\theta_{a/f}}{2}\right) = \frac{\sigma^o_{mid}(\theta_{mid}) - \sigma^o_{a/f}(\theta_{a/f})}{\theta_{mid}-\theta_{a/f}}, \qquad [\mathrm{dB}/deg] \tag{3}$$

Then, slope and curvature values on day d are estimated using all local values distributed over the entire incidence angle range within a 42-day window centered at d (Hahn et al., 2017). The value of λ is chosen to balance the bias and variance of estimates. The performance and robustness of the kernel smoother was tested in Hahn et al. (2017).

2.1.2. Validation data

The open loop (OL) and data assimilation (DA) simulations are compared to the in-situ soil moisture measurements of the International Soil Moisture Network (ISMN; Dorigo et al. (2011, 2013)) at locations illustrated in Fig. 1. ISMN stations were excluded if the percentage of effective time series was <85%. In addition, following Corchia et al. (2023), observations were not assimilated if the SURFEX model indicates the presence of snow or frozen soil based on the initial values of the ice in the second layer (WGI2). The dominant vegetation types at ISMN stations are illustrated in Fig. 1. The ISMN soil moisture measurements are quality controlled, and stations with a data record of less than one year are removed. The relationship between ISMN observations at specific depth and the ISBA simulated soil moisture in various

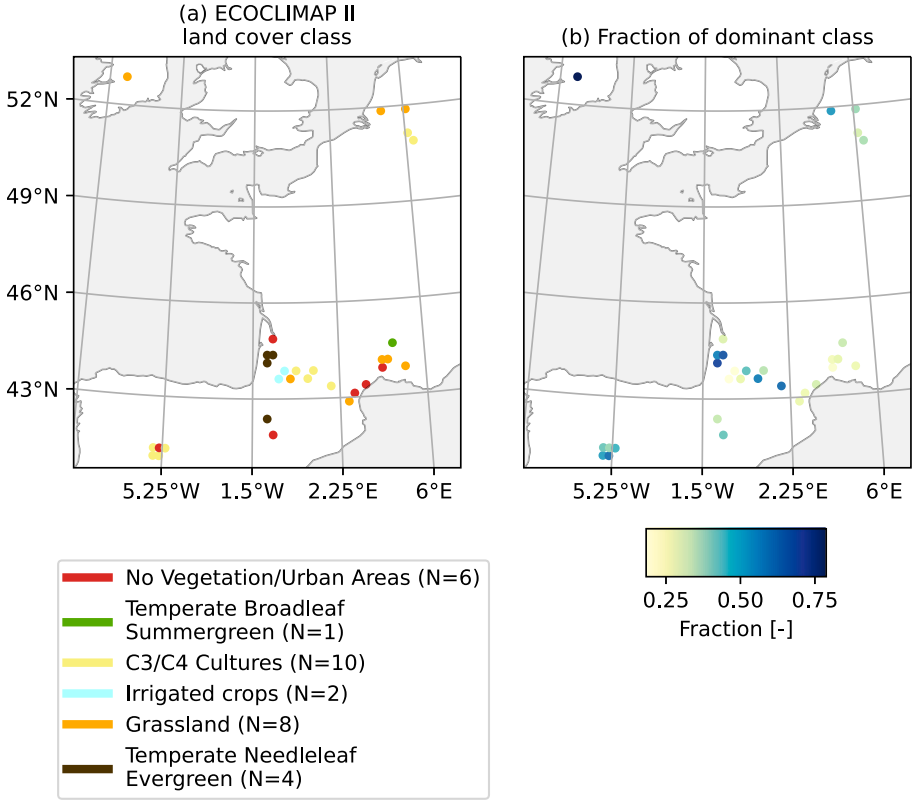

Fig. 1. The main land cover types and fraction of France based on ECOCLIMAP II. (a) the dominant vegetation types of the 0.25° × 0.25° GPIs which contain the ISMN stations; (b) the vegetation fraction of the dominant vegetation types of each GPI. The GPI in Ireland is not included in later calculation of performance metrics due to the short ISMN data record.

layers is shown in Table S1. Root zone soil moisture (RZSM) is calculated as the soil moisture in a layer from 0.1 to 0.4 m because 20 of the 22 ISMN stations have measurements at 0.2 m and 0.4 m. In this study, surface soil moisture (SSM) is defined as soil moisture from 0 to 0.1 m measured at the ISMN station or simulated by the land surface model. A summary of the ISMN stations is provided in Table S3.

The LAI 1 km version 2 products from the Copernicus Global Land Service (CGLS) (Verger et al., 2014) are used as the independent evaluation data. Following Albergel et al. (2017), the 1 km resolution observations are interpolated to the 0.25° model grid points, as long as 50% of the observation grid points are observed. LAI observations have a temporal frequency of about 10 days. LAI from ISBA simulations (both OL and DA) are evaluated against the CGLS LAI on days when the CGLS LAI is available.

2.2. Methodology

2.2.1. ISBA-A-gs model

This study uses the CO2-responsive version of ISBA-A-gs (Interactions between Soil, Biosphere and Atmosphere (Noilhan and Planton, 1989; Noilhan and Mahfouf, 1996), here referred as ISBA) within the SURFEX platform (version 8.1) (Masson et al., 2013; Albergel et al., 2017, 2018). Simulations of dynamics of plant physiological states in land-atmospheric interactions are run with the "NIT" plant biomass monitoring option (Calvet et al., 1998, 2004, 2007). The current ISBA model utilizes Jacob's biochemical A-gs model (Jacobs et al., 1996) to simulate the dynamics of photosynthetic processes responding to changing atmospheric conditions (Albergel et al., 2017). A multi-layer diffusion scheme is used to simulate the dynamics of soil water and temperature (Albergel et al., 2017; Leroux et al., 2018). The ISBA parameters are defined for 19 generic land surface patches as described in Table S2.

The model was forced by the latest ERA5 (ECMWF Reanalysis v5) atmospheric reanalysis from ECWMF (Hersbach et al., 2020) from 1996 to 2019. The meteorological forcing data are available on a 0.25° × 0.25° grid, and include rainfall rate, 2 m air temperature, 2 m specific humidity, wind speed, wind direction, surface pressure, downward direct shortwave radiation, downward diffuse radiation, downward long wave radiation, snowfall rate and CO2 concentration. All ERA5 atmospheric variables were interpolated using bilinear interpolation to match the grid points of ISBA, because the center points of ERA5 grid points are different compared to the center points of ISBA simulations or ASCAT data. The model was initiated by spinning up with 20 repetitions using the 1996 forcing data. The open-loop simulation was obtained using the ERA5 forcing data from 1997 to 2019. Then the data assimilation scheme is run from 1 Jan 2017 to 31 Dec 2019.

2.2.2. Simplified extended Kalman filter

The Simplified Extended Kalman Filter (SEKF) is used to assimilate the ASCAT observables into the LSM ISBA-A-gs. The update equation of SEKF for a single GPI follows:

$$\widetilde{\mathbf{x}}_k^a = \widetilde{\mathbf{x}}_k^f + \widetilde{\mathbf{K}}_k\left(\mathbf{y}_k^o - \mathscr{H}\left(\mathbf{x}_k^f\right)\right) \tag{4}$$

where subscripts a, f, o indicate the analysis, forecast and observation, respectively. The term $\widetilde{\mathbf{x}}_k$ represents the control vector or state vector of dimension (nbp, nbv) computed at time step k, in which nbp indicates the number of patches ISBA-A-gs simulates and nbv is the number of states. The term $\mathbf{x}$ represents the state vector aggregated over different patches which contains LAI, WG2, WG3, WG4, WG5, WG6, WG7, WG8 as described in Table S2. $\mathbf{y}^o$ denotes the observation vector of dimension nbo. $\mathscr{H}$ denotes the non-linear observation operator, i.e. the DNN, which utilizes the input state vector aggregated over different patches within one GPI as well as diagnostic variables. Following Shan et al. (2022), the relevant diagnostic variables are net radiation (RN), vegetation interception reservoir water storage (WR), plant transpiration (LETR), gross primary production (GPP) and stomatal conductance (XRS) (See Table S1). The DNN is trained and tested using data from 2007 to 2016. Jackknife cross-validation is used to choose the best model which minimized RMSE among those submodels according to their performances on the testing dataset. Then the DNN is independently validated from 2017 to 2019 following Shan et al. (2022). The input data of DNN comes from the OL experiment of ISBA from 2007 to 2019. Input land surface variables include the soil moisture in different layers and vegetation-related variables (See Table S1). The DNN is trained independently per GPI to account for the heterogeneity of ASCAT footprints which contain combinations of different patches. The structure of the DNN is tuned by Bayesian optimization (Snoek et al., 2012), including the number of layers, the number of neurons of each layer, batch size, the choice of activation function and learning rate. More details can be found in Shan et al. (2022).

The Kalman gain $\widetilde{\mathbf{K}}_k$ is computed at time k as follows:

$$\widetilde{\mathbf{K}}_k = \begin{pmatrix} \mathbf{K}_{k,[1]} \\ \mathbf{K}_{k,[2]} \\ \cdots \\ \mathbf{K}_{k,[12]} \end{pmatrix} = \widetilde{\mathbf{B}}\widetilde{\mathbf{J}}_k^T\left(\widetilde{\mathbf{J}}_k\widetilde{\mathbf{B}}\widetilde{\mathbf{J}}_k^T + \mathbf{R}\right)^{-1} \tag{5}$$

where $\mathbf{K}_{k,[p]}$ satisfies the update equation for $\mathbf{x}_{[p]}$:

$$\mathbf{x}_{k,[p]}^a = \mathbf{x}_{k,[p]}^f + \mathbf{K}_{k,[p]}\left(\mathbf{y}_k^o - \mathscr{H}\left(\mathbf{x}_k^f\right)\right) \tag{6}$$

and $\widetilde{\mathbf{J}}$ is the Jacobian values of the model ($\mathbf{M}_{k,[p]}$) and the linearized observation operator ($\mathbf{H}_{k,[p]}$) at time step k for patch p, which follows:

$$\widetilde{\mathbf{J}} = \begin{pmatrix} \mathbf{J}_{k,[1]} \\ \mathbf{J}_{k,[2]} \\ \cdots \\ \mathbf{J}_{k,[12]} \end{pmatrix} = \begin{pmatrix} \mathbf{H}_{k,[1]}\mathbf{M}_{k,[1]} \\ \mathbf{H}_{k,[2]}\mathbf{M}_{k,[2]} \\ \cdots \\ \mathbf{H}_{k,[12]}\mathbf{M}_{k,[2]} \end{pmatrix} \tag{7}$$

and $\widetilde{\mathbf{B}}$ is a block diagonal matrix which is "patch-dependently" defined as:

$$\widetilde{\mathbf{B}} = \begin{pmatrix} \mathbf{B}_{k,[1]} & 0 & \ldots & 0 \\ 0 & \mathbf{B}_{k,[2]} & \ldots & 0 \\ \vdots & & \ddots & \vdots \\ 0 & \ldots & 0 & \mathbf{B}_{k,[12]} \end{pmatrix} \tag{8}$$

Here, the background error matrix is defined as "patch-dependent" because the model uncertainty for LAI is calculated based on the value of LAI in the different patches. The values of $\mathbf{B}_{k,[p]}$, $p = 1, \ldots, 12$ are defined following Mahfouf et al. (2009), Draper et al. (2011), and Albergel et al. (2017). The background errors of soil moisture are assumed to be proportional to the dynamic range (the difference between the volumetric field capacity w_{fc} and the wilting point w_{wilt}), which is determined by the soil texture (Noilhan and Mahfouf, 1996). In this study, the perturbation applied on the states of soil moisture in the calculation of the Jacobian matrix were assigned as $1 \times 10^{-4} \times \left(w_{fc} - w_{wilt}\right)$ following Albergel et al. (2017), and $0.001 \times LAI$ for LAI. For volumetric surface soil moisture, a mean standard deviation (SD) error of 0.04 m^3m^{-3} is prescribed. For soil moisture in deeper layers, SD error of 0.02 m^3m^{-3} is used following Mahfouf et al. (2009), Draper et al. (2011), Barbu et al. (2011), and Barbu et al. (2014). The observation error for σ_{40}^o is set as 0.33 dB following Lievens et al. (2017a) and 0.005 dB/deg. for $\sigma^{'}$ following Wagner et al. (1999a) and Hahn et al. (2017).

The control vector evolution from time k to the end of the 12 h assimilation window (k + 1) follows:

$$\widetilde{\mathbf{x}}_{k+1,[p]}^f = \mathscr{M}_{k,[p]}\left[\widetilde{\mathbf{x}}_{k,[p]}^a\right] = \widetilde{\mathbf{M}}_{k,[p]}\widetilde{\mathbf{x}}_{k,[p]}^a \tag{9}$$

where $\mathscr{M}_{k,[p]}$ denotes the LSM ISBA-A-gs at time k at patch p. The term $\widetilde{\mathbf{M}}_{k,[p]}$ is the linearization of $\mathscr{M}_{k,[p]}$ at patch p. For σ_{40}^o, the assimilation is done every 24 h at 10 am. For $\sigma^{'}$, daily values are assimilated per 24 h.

By definition, the Kalman gain in Eqs. 4 and 7 would be optimal if the modeling process in Eq. (9) is linear, and the model and observation noises are zero mean and uncorrelated white noise with correctly specified covariance $\widetilde{\mathbf{B}}$ and $\mathbf{R}$ respectively (Reichle et al., 2017b). In this case, the SEKF estimates would provide the best least-squared estimates of the updated states given the value of the OL results, observations, model errors and observation errors (Kailath, 1968). Section 2.2.3 introduces the diagnostics used to determine the degree to which these assumptions are valid, and therefore whether the DA system is optimal.

2.2.3. Performance metrics and diagnostics

The performance of the DA and OL are evaluated using unbiased root mean square error (ubRMSE, (Entekhabi et al., 2014)), bias and the Pearson correlation coefficient (ρ) against the ISMN observations and CGLS LAI observations. Additionally, the normalized information contribution (NIC, Albergel et al. (2018)) is used on ubRMSE and ρ to quantify the relative improvement or degradation of DA compared to OL estimates of states. The NIC is calculated for ubRMSE and ρ as follows. These metrics provide a measure of the percentage change (negative NIC for ubRMSE or positive NIC for ρ) or degradation (positive NIC for ubRMSE or negative NIC for ρ) in ubRMSE and ρ achieved by the DA system compared to the OL estimates.

$$NIC_{ubRMSE} = \frac{ubRMSE_{DA} - ubRMSE_{OL}}{ubRMSE_{OL}} \times 100 \tag{10}$$

$$NIC_{\rho} = \frac{\rho_{DA} - \rho_{OL}}{1 - \rho_{OL}} \times 100 \tag{11}$$

The evaluation of ISBA simulations against ISMN measurements follows the best practices outlined by Gruber et al. (2020) and used by e.g. Barbu et al. (2014); Lannoy and Reichle (2016a, 2016b), Lievens et al. (2017a). If a GPI contains a single ISMN station, the in-situ soil moisture measurements from the ISMN station are directly compared to the ISBA simulations (open loop and data assimilation experiments). For grid points containing multiple ISMN stations, the soil moisture measurements from all ISMN sites are weighted and averaged, taking into account the land cover at the ISMN site and the fractional cover of that type ISBA within the GPI.

The impact of data assimilation can be analyzed and diagnosed in the observation space. All diagnostics are summarized in Table 1 along with the corresponding hypothesis and references. In an optimally calibrated and linear system that satisfies the assumptions outlined in section 2.2.2, the innovations (observation-minus-forecast, O—F) are zero-mean white noise. This reflects an unbiased analysis that effectivelty extracts all information from the observations (Daley, 1992). To test this hypothesis, the time series mean and lagged autocorrelation of the innovations are calculated. Autocorrelations at lags from 1 to 10 days are considered. Specifically, Daley (1992) demonstrates that the autocorrelation at a lag of 1 day (C^k_{k+1}) reflects the optimality of the Kalman gain. The optimality of the Kalman gain is achieved when the model and observation operator are linear and there is no misspecification of the forecast (or model) and observation errors (Daley, 1992). Consider the lagged innovation covariance matrix C^k_{k+1} at time step k defined as eq. (2.12) in Daley (1992),

$$C^n_{n+1} = \widetilde{\mathbf{J}}_k \left[\widetilde{\mathscr{B}} \widetilde{\mathbf{J}}^T - \widetilde{\mathbf{K}}_k \left(\widetilde{\mathbf{J}}_k \widetilde{\mathscr{B}} \widetilde{\mathbf{J}}^T_k + \mathcal{R} \right) \right] \tag{12}$$

where $\widetilde{\mathbf{K}}$ is the estimated Kalman gain from 7, $\widetilde{\mathscr{B}}$ and $\mathcal{R}$ are the correctly specified model and observation errors, respectively. If the DA system is optimal, then the estimated Kalman gain is equal to the optimal Kalman gain, i.e. $\widetilde{\mathscr{K}}_k = \widetilde{\mathscr{B}} \widetilde{\mathbf{J}}^T \left[\widetilde{\mathbf{J}}_k \widetilde{\mathscr{B}} \widetilde{\mathbf{J}}^T_k + \mathcal{R} \right]^{-1}$.

If the lagged innovation covariance is close to zero, it indicates that the Kalman gain matrix is optimal (Kailath, 1968; Daley, 1992) and the DA system extracts most of the available information from the observations. Conversely, the observations are not used efficiently if the lagged autocorrelation values are large.

Moreover, if the model errors and observation errors are uncorrelated and normally distributed, the standard deviation of the innovations should be equal to the sum of the covariance of the model forecast and observation errors with correctly specified model and observation error (Reichle et al., 2002a; Desroziers et al., 2005; Barbu et al., 2011; Reichle et al., 2017b). That is,

$$E\left[\left(\mathbf{y}^o_k - \mathscr{H}\left(\mathbf{x}^f_k \right) \right) \left(\mathbf{y}^o_k - \mathscr{H}\left(\mathbf{x}^f_k \right) \right)^T \right] = \mathbf{R} + \widetilde{\mathbf{J}}_k \widetilde{\mathbf{B}} \widetilde{\mathbf{J}}^T_k \tag{13}$$

The term on the left hand side represents the actual errors encountered in the DA systems while the right hand side contains the prescribed, assumed errors. Thus, the time series standard deviation values of the normalized innovations (normalized observation-minus-forecast or normalized O—F) are computed as:

$$\text{std}(\text{normalized innovations}) = \text{std}\left(\frac{\mathbf{y}^o_k - \mathscr{H}\left(\mathbf{x}^f_k \right)}{\sqrt{\mathbf{R} + \widetilde{\mathbf{J}}_k \widetilde{\mathbf{B}} \widetilde{\mathbf{J}}^T_k}} \right) \tag{14}$$

Values of this standard deviation greater than one indicate that the DA system underestimates the actual errors (observation error and forecast error), and values less than one indicate that the actual errors are overestimated. Note that the diagnostic only addresses the total error and does not distinguish between observation and forecast errors.

Another useful diagnostic is the residual (Observation-minus-analysis, or O-A), which is defined as the difference between the observation and the observation equivalent predicted from the updated states. In a well-calibrated system, the time series mean values of the residuals should be zero. The time series standard deviations of residuals should be smaller than the time series standard deviations of innovations, which would reflect a reduction of uncertainty in the estimated observation equivalent in the observation space (Reichle et al., 2017b).

The analysis impact is also assessed using the absolute value of the ratio of the residuals to the innovations, i.e. $|(O-A)/(O-F)|$ (Kolassa et al., 2017). The absolute values of residuals should be smaller than the innovations. This means that the observation equivalent($\mathbf{y}^a$) of the analysis ($\mathbf{x}^a$) should be closer to the true observation $\mathbf{y}^o$ compared to the observation equivalent ($\mathbf{y}^f$) of the forecast ($\mathbf{x}^f$) (Kolassa et al., 2017).

Table 1
Summary of diagnostics along with the corresponding hypothesis and references.

Diagnostics	Ideal values	Hypothesis	References
mean(innovations)	0	The innovations are zero-mean white noise	Kailath (1968), Daley (1992), Reichle et al. (2017b)
mean(residuals)	0	The system is well-calibrated	Reichle et al. (2017b)
std(innovations) - std.(residuals)	> 0	The DA reduces the uncertainty	Reichle et al. (2017b)
Autocorrelation of innovations lagged on different days	0	The innovations are zero-mean white noise and the Kalman gain is optimal	Daley (1992), Reichle et al. (2017b)
std(normalized innovations)	1	The actual errors are well prescribed	Reichle et al. (2002a), Desroziers et al. (2005), Barbu et al. (2011), Reichle et al. (2017b)
mean$\lvert O-A/O-F\rvert$	< 1	The DA system is effective	Kolassa et al. (2017)

Thus the mean ratio of $|(O-A)/(O-F)|$ should be smaller than 1. In the scalar case, this ratio is equal to 1 - $\widetilde{\mathbf{K}}_k$ where $\widetilde{\mathbf{K}}_k$ is the Kalman gain. Values smaller than 1 indicate that the DA system is effective.

3. Results

3.1. Performance

3.1.1. Performance across all GPIs

In Fig. 2, scatter plots of ubRMSE, bias and ρ are shown to evaluate the performances of the DA and OL experiments against the in-situ ISMN soil moisture and CGLS LAI observations. Summary statistics are reported in Table 2.

Regarding LAI, the median value of ubRMSE from the OL across GPIs is 0.58 m^2m^{-2}. The spatially median value of NIC of ubRMSE for LAI is 2.2%. While the positive NIC values indicate that the DA is making the LAI estimate worse, the magnitude of the degradation is so small that the impact is effectively neutral. For bias, the median value across GPIs is −0.23 m^2m^{-2} for the OL and −0.30 m^2m^{-2} for the DA. The magnitude of the bias is slightly changed but all GPIs are centered around the 1:1 line. This is because SEKF is bias-blind data assimilation algorithm, so that SEKF only reduces the random noise in states rather than correcting the bias (Dee, 2005). For ρ, most agricultural GPIs fall below the 1:1 line in the scatter plots. Fig. 2 (c) shows that DA reduces the ρ of LAI for most GPIs. Fig. 3 (a) provides some insight as to why. The estimated LAI from the OL does not capture the seasonal cycle observed by the CGLS LAI. While DA clearly impacts the estimated LAI, it does not lead to an improvement with respect to the independent observations.

For SSM (WG3), the median values across all GPIs of ubRMSE from the OL is 0.04 m^3m^{-3}. In general, the DA updates are neutral on agricultural and grassland GPIs, and the median value across all GPIs of NIC is too small (−0.22%) so that the updates have nearly zero effects. The median values across GPIs of bias from the OL and DA are −0.081 m^3m^{-3} and − 0.082 m^3m^{-3}, respectively. Bias barely changes because SEKF does not correct bias. However, the potential for improvement may be limited by the already excellent performance of the OL simulations, with ubRMSEs values generally below 0.05 m^3m^{-3}. For RZSM (WG4&WG5), the median values of ubRMSE OL across GPIs is 0.029 m^3m^{-3}. The median values across GPIs of bias from the OL and DA are −0.084 m^3m^{-3} and − 0.085 m^3m^{-3}, respectively. The DA does not change the bias compared to ISMN measurements. The DA makes limited improvements in terms of ubRMSE and ρ.

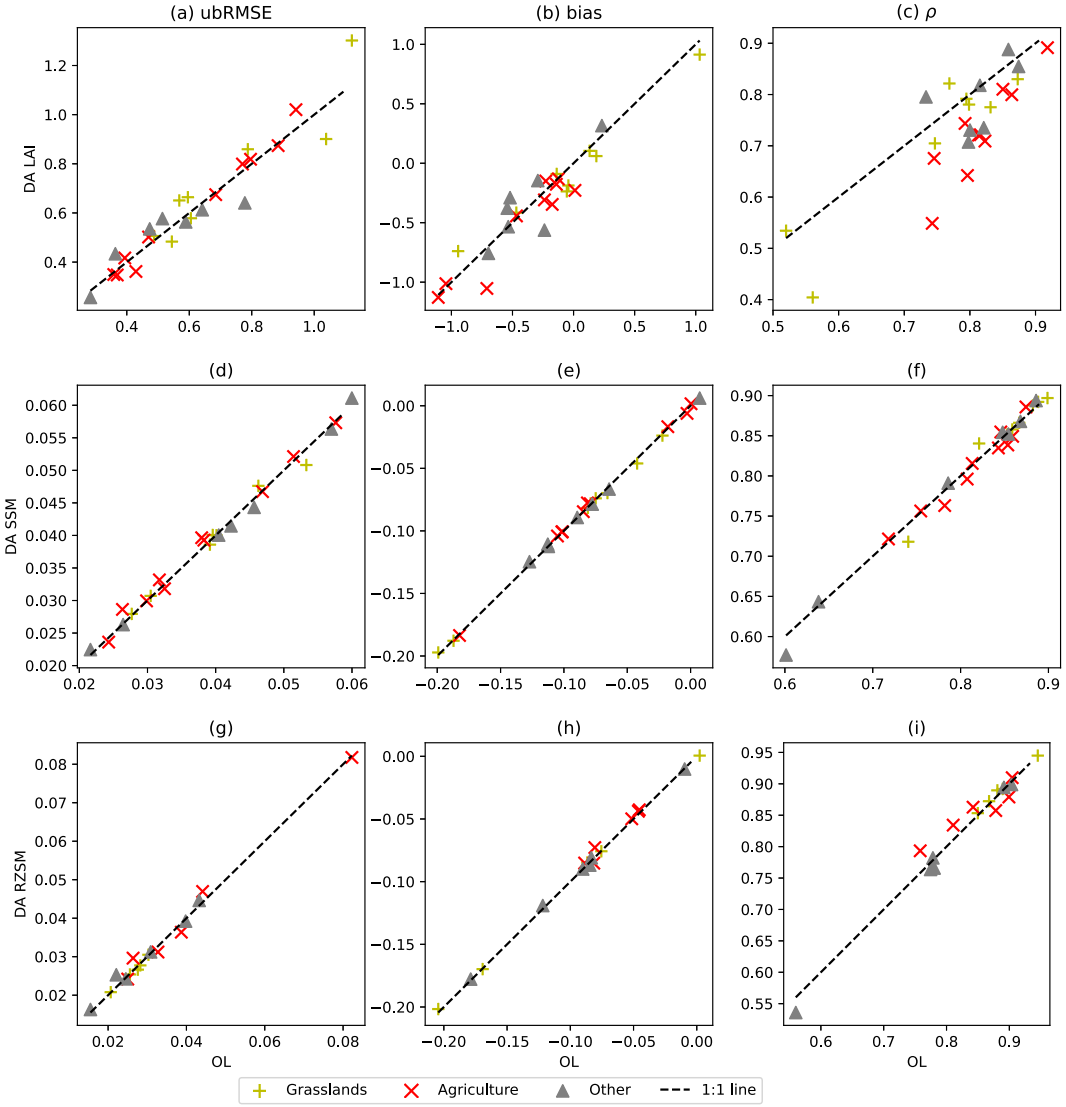

Fig. 2. Scatter plot of the ubRMSE, bias and Pearson correlation coefficient for LAI, SSM (WG3, 0.04 m - 0.1 m soil moisture), RZSM (WG4&WG5, 0.1 m - 0.4 m) for OL and DA(σ^o_{40}, $\sigma^{'}$) evaluated against in-situ ISMN observations and Copernicus LAI observations from 2017 to 2019. Agricultural GPIs are marked as 'x', grasslands GPIs as'+' and other GPIs as triangles. The absence of some stations of RZSM is due to the lack of sensors at some depths in the ISMN at some stations.

Table 2
Statistics of performances of OL and DA averaged across all GPIs, grassland GPIs and Agriculture GPIs.

	all GPIs	Grassland	Agriculture
LAI			
OL ubRMSE (m^2m^{-2})	0.58	0.6	0.58
DA ubRMSE (m^2m^{-2})	0.58	0.66	0.59
NIC ubRMSE	2.2	6.5	0.81
OL ρ	0.81	0.78	0.81
DA ρ	0.76	0.78	0.72
NIC ρ	−6.5	−3.6	−10
SSM (WG3)			
OL ubRMSE (m^3m^{-3})	0.04	0.04	0.035
DA ubRMSE (m^3m^{-3})	0.04	0.04	0.036
NIC ubRMSE	−0.22	0.8	0.82
OL ρ	0.85	0.87	0.83
DA ρ	0.85	0.87	0.83
NIC ρ	0.027	−0.069	−0.38
RZSM (WG4&WG5)			
OL ubRMSE (m^3m^{-3})	0.029	0.028	0.036
DA ubRMSE (m^3m^{-3})	0.03	0.027	0.034
NIC ubRMSE	−0.51	−0.74	−1.9
OL ρ	0.87	0.88	0.86
DA ρ	0.87	0.89	0.86
NIC ρ	0.3	0.41	1.5

3.1.2. States at agricultural GPIs

Fig. 3 shows the time series of DA, OL and observations of LAI, SSM (WG3), RZSM (WG4 & WG5), WG6, WG7, and WG8 averaged over the agricultural GPIs in southwestern France (The Saint Felix de Lauragais, Lahas, Condom and Savenes stations from the SMOSMANIA network). Their geographical proximity allows us to average their statistics. Both the OL and DA estimates of LAI are higher than the CGLS LAI observations. The assimilation lowers the LAI values during the spring of 2017 and summer of 2019. The assimilation of σ^o_{40} results in negative increments of LAI from Jan to April in 2017 and from March to July 2019. During these periods, the ratios of residual to innovation of σ^o_{40} are reduced (Fig. 4 (a)). In May 2017, the update of LAI is primarily due to the assimilation of $\sigma^{'}$. The residual/innovation of $\sigma^{'}$ is less than unity during this period (Fig. 4 (b)). The DA draws the LAI towards the CGLS LAI by the negative innovations of $\sigma^{'}$ (Fig. 4 (b)) with positive J($\sigma^{'}$, LAI) (Fig. 9 (j)).

From Fig. 3, DA has little to no effect on SSM (WG3) and RZSM (WG4&WG5) at these stations. The ubRMSE of the OL is already small, so the SSM (WG3) cannot be improved much. The OL cannot be improved much. The difference between both OL and DA results and the in situ observations could partly be explained by representativeness error due to the mismatch in scales between the in situ, point-scale observations and the OL and DA estimates which are at $0.25^\circ \times 0.25^\circ$. This mismatch results in large bias between ISBA simulations and ISMN measurements and the SEKF does not correct this bias. Note that the DA creates wetter estimates of the RZSM (WG4&WG5) compared to the OL in Sep 2019. This is attributed to the negative J(σ^o_{40}, RZSM) (Fig. 9 (c)) and negative innovations of σ^o_{40} shown in Fig. 4 (a).

It is noticeable that both of the OL and DA simulations of SSM and RZSM (WG4 & WG5) have a different dynamic range compared to ISMN in-situ measurements. This systematic bias is due to the fact that soil moisture data from different sources (LSM simulations, satellite retrievals, ground measurements) exhibit different climatologies though they contain consistent information about soil water dynamics (Reichle and Koster, 2004). Therefore, ubRMSE is used as the performance metric to reflect the root mean square error of time series anomalies that are computed by removing the mean (Entekhabi et al., 2014). This is also used in previous studies when evaluating the DA results against in-situ measurements (Barbu et al., 2014; Albergel et al., 2017, 2018; Lannoy and Reichle, 2016b,a; Lievens et al., 2017a, 2017b). Meanwhile, we separated ISMN in-situ measurements into a twin axis in Fig. 3. This is to emphasize that the dynamics between ISBA and ISMN data are comparable, and the differences in ranges of ISBA simulations and ISMN measurements are primarily related to different climatologies. However, it is essential to pay attention to the representativeness error in the dynamics, because ground-based measurements are sparse and not necessarily representative of large-scale soil moisture simulations (Reichle et al., 2004).

WG6, WG7 and WG8 are pushed towards drier estimates from October 2018 to May 2019. This starts from October 16, 2018, after which Fig. 4 (a) shows that residual/innovation of σ^o_{40} reaches a local minimum. A similar situation occurs on Jan 27 2019, when the updates of WG6, WG7 and WG8 are driven by the assimilation of σ^o_{40}. In this case, DA reduces the ratio of residual to innovations of σ^o_{40} more than $\sigma^{'}$. Note that soil moisture in deeper layers have larger increments from October 2018 to May 2019. This is due to the larger sensitivities of the observations to deeper WGs as shown in Fig. 8 (b), (e), (c) and (f).

3.2. Data assimilation diagnostics

3.2.1. Innovations and residuals

Fig. 5 (a-b) and (e-f) show the time series mean and standard deviation of innovations (observation-minus-forecast, O—F). The median and standard deviation across all GPIs are reported in Table 3. The time series mean values of innovations are typically small and range from −0.17 dB to 0.25 dB for σ^o_{40} and from −0.0025 dB/deg. to 0.0028 dB/deg. for $\sigma^{'}$. Overall, the median values across GPIs are 0.018 dB for σ^o_{40}, and 0.00055 dB/deg. for $\sigma^{'}$. For most GPIs, there is small positive bias of σ^o_{40} and $\sigma^{'}$, with fewer stations exhibiting negative mean innovations values. Small values of the time series mean of innovations suggest that the assimilation system is nearly bias-free. For residuals, the time mean values of residuals range from −0.15 dB to 0.25 dB for σ^o_{40} and from −0.0023 dB/deg. to 0.0026 dB/deg. for $\sigma^{'}$. Generally there is small positive bias of 0.031 dB for σ^o_{40} and 0.00041 dB/deg. for $\sigma^{'}$. The time mean values of residuals have smaller median values across GPIs and range compared to the innovations.

The time series standard deviation of innovations range from 0.17 dB to 0.52 dB for σ^o_{40} and from 0.0032 dB/deg. to 0.0076 dB/deg. for $\sigma^{'}$. The median value across GPIs is 0.29 dB for σ^o_{40} and 0.0047 dB/deg. for $\sigma^{'}$. High values are found in GPIs containing REMEDHUS stations in Spain, where the main land cover type is agricultural. This may also be related to the fact that the subsurface scattering effects may be present in GPIs containing REMEDHUS stations (Wagner et al., 2022). The standard deviation of innovations of $\sigma^{'}$ are also higher in GPIs in southwestern France. At these GPIs, σ^o_{40} and $\sigma^{'}$ typically exhibit strong variability as shown in Fig. S1 (c) and (d). The median value across GPIs of the time series standard deviation of residuals is 0.27 dB and 0.0047 dB/deg. for σ^o_{40} and $\sigma^{'}$, respectively, which is smaller than the innovations. This reduction represents the impact of the ASCAT observations on the DA system, i.e. a decrease in the uncertainties following the assimilation of ASCAT σ^o_{40} and $\sigma^{'}$. However, the fact that these reductions are generally small across all GPIs suggests that the DA framework is too conservative in updating the states in observation space.

3.2.2. Prescribed errors and the impact of DA

Fig. 6 (a-b) shows the standard deviation of the normalized innovations which measures the consistency between prescribed errors and the actual errors in the data assimilation system (Reichle et al., 2017b). Overall, the median values across GPIs of the metric are smaller than 1 with values of 0.83 for σ^o_{40} and 0.87 for $\sigma^{'}$). This suggests that, in general, the magnitudes of pre-assumed model and observation errors tend to overestimate the magnitudes of prescribed model errors. This

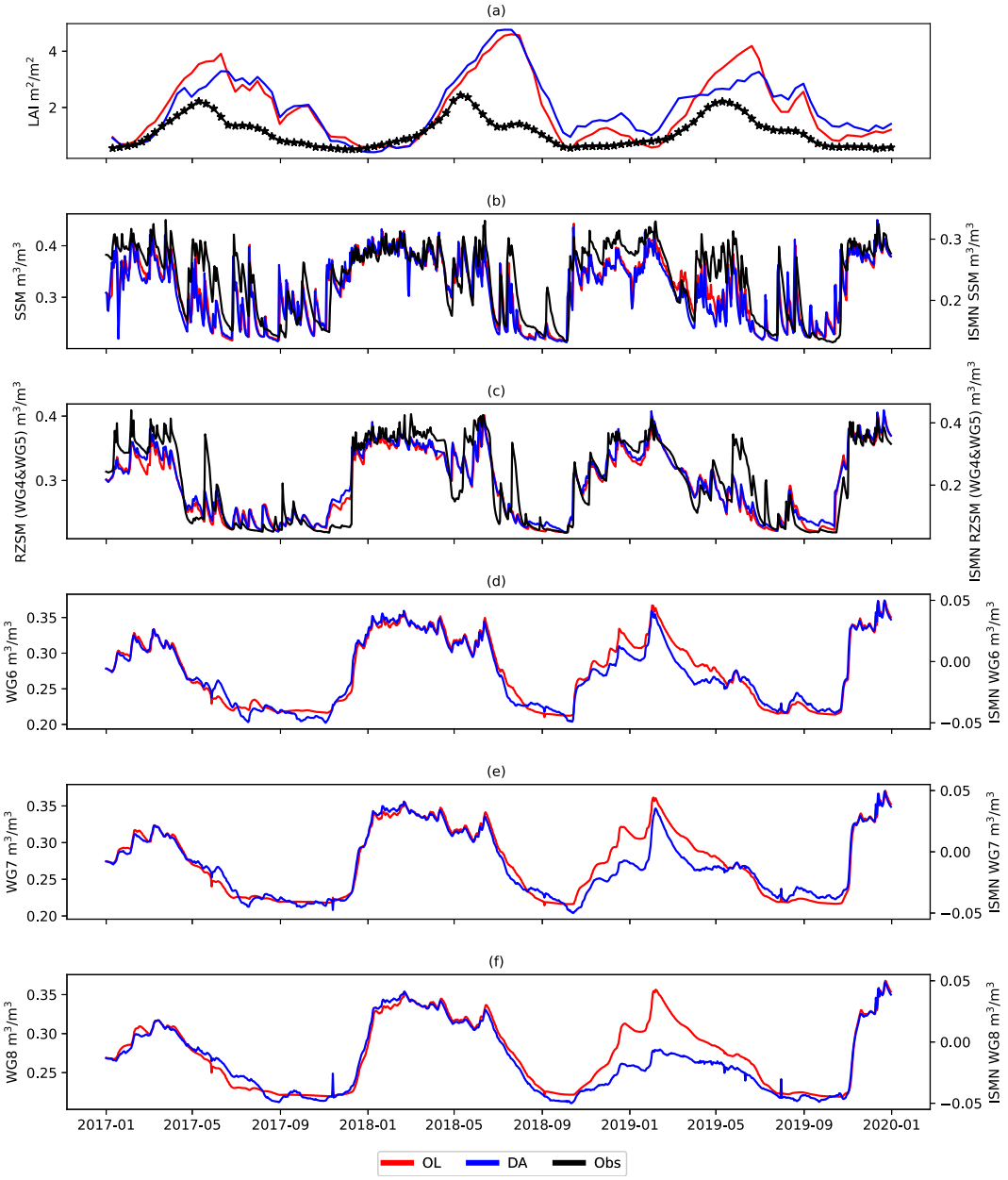

Fig. 3. Time series of LAI, WG3 (0.04 m - 0.1 m soil moisture), root zone soil moisture (RZSM, 0.1 m - 0.4 m) for observation, OL and DA(σ^o_{40}, $\acute{\sigma}$) from 2017 to 2019, averaged on agri GPIs in southwestern France (GPIs containing ISMN stations: Saint Felix de Lauragais, Lahas, Condom and Savenes in SMOSMANIA network). Simply averaging all agricultural GPIs might suffer from different weather conditions which shapes different time series behaviours in soil moisture curves.

metric varies considerably, particularly with land cover type. Specifically, agricultural GPIs have larger values of the metric compared to grassland GPIs. In grassland GPIs, the median values across GPIs are 0.68 for σ^o_{40} and 0.7 for $\acute{\sigma}$, indicating that the prescribed model and observation errors overestimate one or both of the actual errors. In contrast, on agricultural GPIs, the spatial median value is 1 for σ^o_{40} and 0.78 for $\acute{\sigma}$, suggesting that overestimation is less of an issue in agricultural GPIs.

Additionally, note that the spatial standard deviation of the metric is larger for $\acute{\sigma}$ than for σ^o_{40}. This difference could be partially due to the use of spatially constant observation errors for σ^o_{40} and $\acute{\sigma}$. This does not capture any spatial variability in observation error due to e.g. heterogeneity, land cover type, etc. As a result, the degree of overestimation varies across different GPIs.

Fig. 6 (c-d) show the mean values of $|\frac{O-A}{O-F}|$ for σ^o_{40} and $\acute{\sigma}$. This quantifies the impact of data assimilation by assessing the correction of observation equivalents from the forecast to the true observations. Values range from 0.75 to 0.99 for σ^o_{40} and 0.58 to 0.99 for $\acute{\sigma}$. Overall, the median values across GPIs of $|\frac{O-A}{O-F}|$ are 0.92 for σ^o_{40} and 0.86 for $\acute{\sigma}$. Values of the metric are smaller than 1, indicating that the data assimilation is effective in improving the observation equivalents. However, the values are relatively close to unity. This suggests that the analysis assigns similar weights to the observations and ISBA model (Kolassa et al., 2017). The metric varies across the GPIs. In particular, the ratios are generally smaller for agricultural GPIs compared to grassland GPIs for σ^o_{40} and $\acute{\sigma}$ as shown in Table 3. This suggests that DA is much more effective in agricultural GPIs. This may be due to the more dynamic soil moisture and LAI cycles of crops compared to grass, reflected by the larger standard deviations of σ^o_{40} and $\acute{\sigma}$ shown in Fig. S1 (c) and (d).

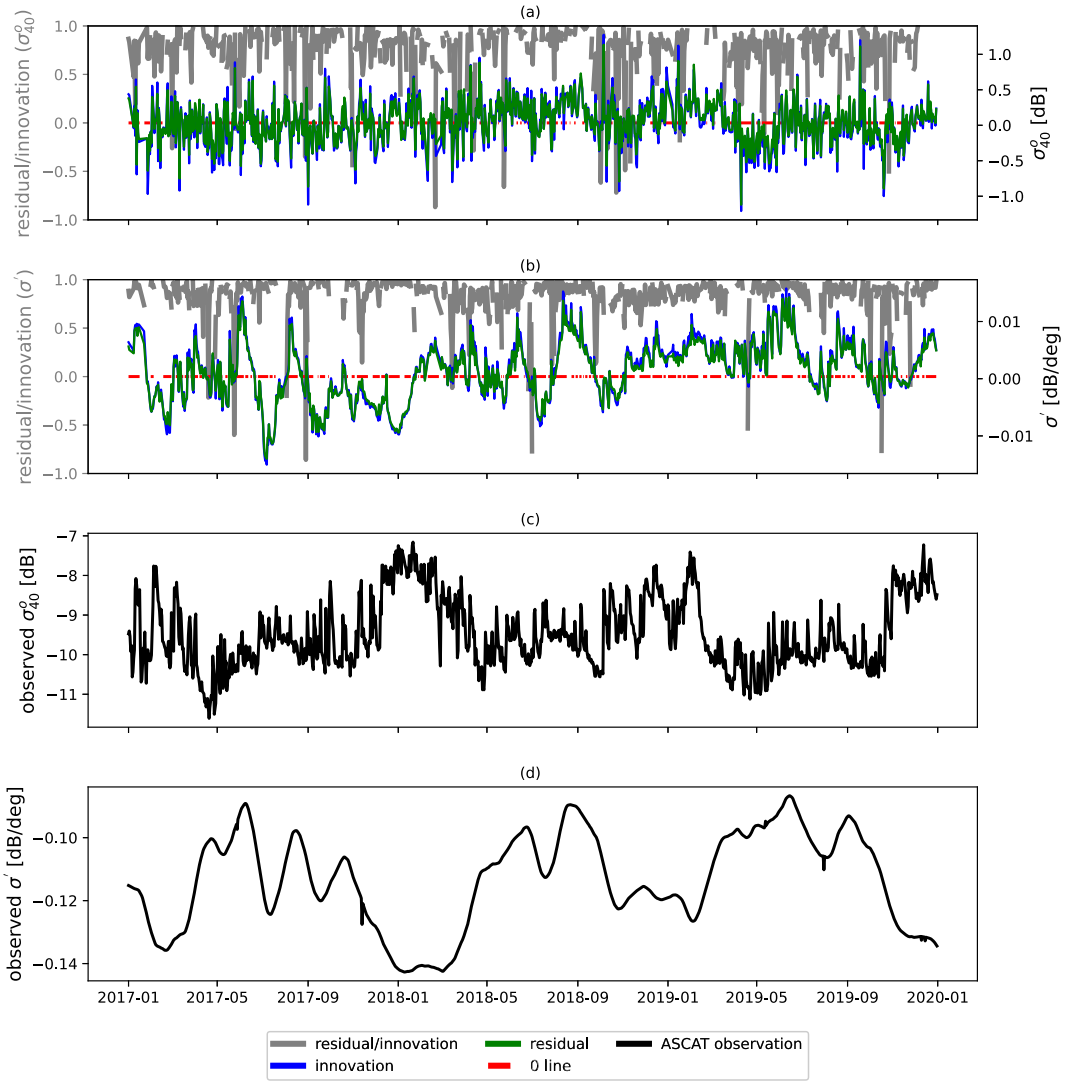

Fig. 4. Time series plot innovations (blue line), residuals (green line) and the ration of residuals (grey line) of a) σ^o_{40} and b) σ' from 2017 to 2019, averaged on agri GPIs containing ISMN stations: Saint Felix de Lauragais, Lahas, Condom and Savenes in SMOSMANIA network. (For interpretation of the references to colour in this figure legend, the reader is referred to the web version of this article.)

3.2.3. *Optimality of the DA system*

Fig. 7 shows autocorrelations of innovations for σ^o_{40} and σ' at lags from 1 to 10 days. Autocorrelation values are significantly >0 at the 5% significance level, though they decrease as the lag increases. Overall, the large autocorrelation values suggest that the innovations are not white noise. This suggests suboptimal performance of the DA system (Daley, 1992), so that the DA system is not making optimal use of the ASCAT observations. The lagged autocorrelation values are larger on grassland GPIs than other GPIs. This suggests, consistent with the previous paragraph, that the DA system is more suboptimal for grasslands than other cover types. The autocorrelation for a lag of 1 day (C^k_{k+1}) depends on the deviations between the optimal weight $\widetilde{\mathscr{K}}$ and the estimated weight $\widetilde{\mathbf{K}}$ (Daley, 1992). The statistics of C^k_{k+1} are also reported in Table 3. The median value across GPIs of C^k_{k+1} is large with the value of 0.37 for σ^o_{40} and 0.83 for σ'. This shows that the system is more suboptimal for σ' compared to σ^o_{40}. In our DA system, both model and observation errors deviate from the actual errors as shown in Fig. 6. The overestimation of the term $\widetilde{\mathbf{J}}_k\widetilde{\mathbf{B}}\widetilde{\mathbf{J}}^T_k + \mathbf{R}$ leads to positive C^n_{n+1} values in Fig. 7. This is one of the reasons why the DA system is suboptimal. However, particular attention needs to be paid to the interpretation of innovation correlation pattern in our DA system. The nonlinearity of the DNN should be considered, as it might contribute to the uncertainty during the assimilation process. Uncertainty associated with DNN's ability to capture the relationship between ASCAT observations and model states, might lead to the suboptimality of the DA system through their impact on eq. (25) in Kailath (1968). Additionally, σ' is estimated by combining all local slope measurements using an Epanechnikov kernel with a half-width of 42 days, which may introduce autocorrelation of the innovation of σ' (Melzer, 2013; Hahn et al., 2017).

4. Discussion

The limited effect of DA may be connected to inconsistency between the Jacobians relating the ASCAT observables to soil moisture in the different layers. The soil moisture in the various layers are highly correlated, so it is reasonable to expect that the Jacobians (or the NSCs) for the different layers would be similar, at least in sign. Fig. 8 shows the NSC of ASCAT σ^o_{40} and σ' to RZSM (WG4&WG5) and soil moisture in the other layers. NSC(σ^o_{40}, WG3) exhibits the expected behaviour, i.e. a positive value in winter. In summer, NSC(σ^o_{40}, WG3) fluctuates around zero, suggesting σ^o_{40} loses sensitivity to WG3 because of the presence of

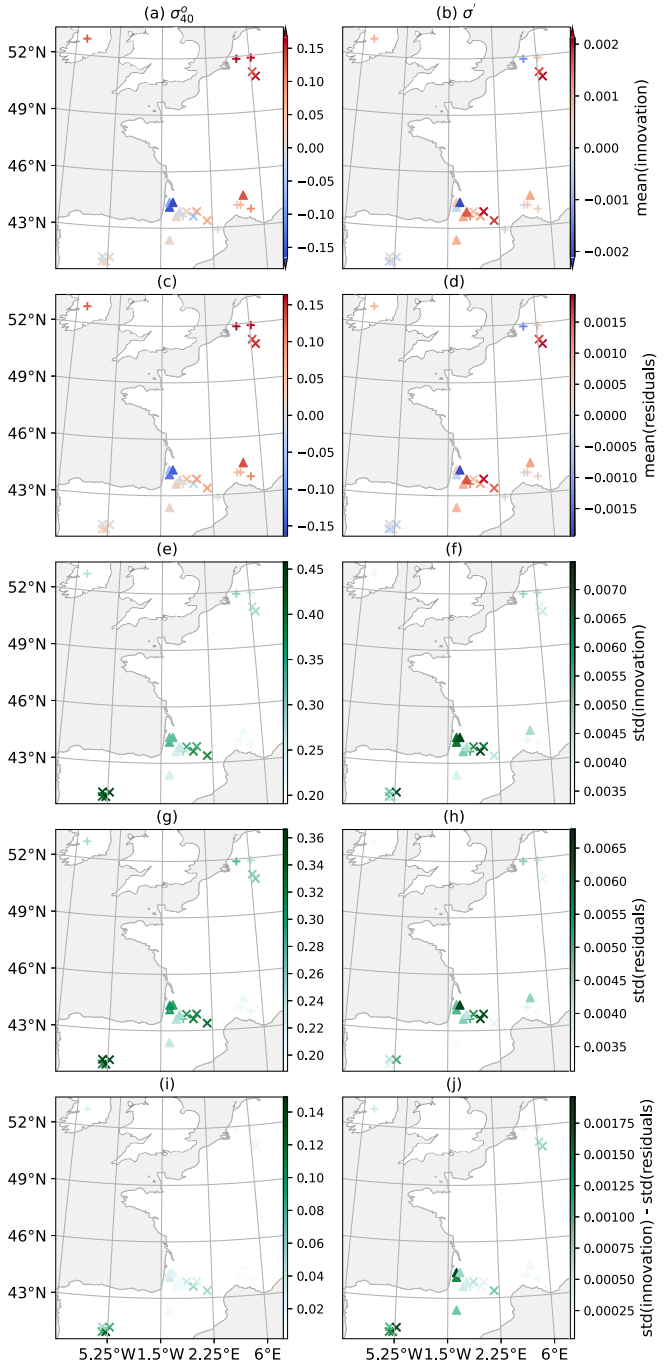

Fig. 5. Diagnostics of DA(σ^o_{40}, σ') from 2017 to 2019. Different rows show mean values of innovations and residuals, standard deviations of innovations and residuals, as well as the difference between std. of innovations and std. of residuals. Different rows show different observations (σ^o_{40} and σ'). Agricultural GPIs are marked as 'x', grasslands GPIs as'+' and other GPIs as triangles.

vegetation. However, this is not the case for the soil moisture in deeper layers. NSC(σ^o_{40}, WG6) oscillates more than the NSCs for shallower layers during the fall and winter in 2017 and the fall in 2019. This is not plausible because WG6 is a damped and delayed with respect to WG3-WG5. This suggests that the DNN may arbitrarily choose among the soil moisture layers during the training process to fit the observed σ^o_{40}.

From Fig. 3 it is clear that the soil moisture series in adjacent layers (WG6, WG7 and WG8) are highly-correlated. Meanwhile, Fig. 8 shows that the normalized sensitivity coefficients for each observation (σ^o_{40} or σ') with respect to WG5, WG6 and WG7 vary considerably and often in opposite directions. These layers are sufficiently deep that their soil moisture content should not have any influence on ASCAT σ^o_{40}. However, Fig. 8 shows that the DNN-estimated σ^o_{40} varies with WG7, and to a lesser degree with WG6. Collectively, these figures suggest that the DNN is overfitting using WG6 and WG7. Therefore, the DNN has been trained to use WG6 and WG7 to adjust σ^o_{40}, resulting in non-zero Jacobian terms for σ^o_{40} and the deep soil moisture states (WG6 and WG7). When these Jacobians are subsequently used in the SEKF, they introduce spurious sensitivity to deep soil moisture and therefore poor DA performance.

The divergent sensitivities have a direct impact on the the robustness of the Jacobian matrix (J) in the SEKF update eq. 4. Fig. 9 shows the J terms aggregated over patches in eq. (7) from 2017 to 2018. Note that here J represents the product of the linearization of ISBA and the Jacobian of the DNN. It is noticeable that the J(σ^o_{40}, WGs) and J(σ', WGs) diverge. The J(σ^o_{40}, WGs) values are positive in spring and become negative in summer and autumn. For σ', J is quite consistent for SSM (WG3) and RZSM (WG4&WG5) but diverges for WG6, WG7 and WG8. The magnitude of the J matrix of WG6, WG7 and WG8 are the largest among the soil moisture. This partly explains why increments on WG6, WG7 and WG8 are so large compared to those in the layers closer to the surface.

Results from Fig. 6 suggested that the (total) observation and model errors were overestimated, something which would limit the efficacy of assimilation. Rather than reducing the prescribed model errors, which are consistent with those in previous SURFEX studies, we reduced the observation errors assumed for the ASCAT observables to investigate if this rendered the DA system more optimal. For the same four agricultural GPIs considered in Fig. 3, the DA experiments were repeated assuming observation errors of 0.15 dB for σ^o_{40} and 0.002 dB/deg. for σ'. The performance metrics and DA diagnostics are reported in Table S4 and S5. The mean values of $|\frac{O-A}{O-F}|$ are reduced, indicating that the DA system tends to follow the observation more than the LSM. The C^k_{k+1} values of innovations are also reduced. So, reducing the observation errors results in a less sub-optimal DA system. However, while the magnitudes of the NIC values increase, the sign of the NIC values do not change on most cases. GPIs at which DA improved state estimates show a stronger improvement. However, GPIs where DA proved detrimental have a worse performance when the observation error is reduced. Despite the tighter constraints imposed by the observations, the sign of the increments did not change. Instead, it appears that the Jacobians of the observation operator, which establish the link between the land surface variables and the ASCAT observations, had a larger impact on the DA system. While the observation error controls the magnitude of the increments, the Jacobian terms determine the sign of the increments, as shown in Figs. 8 and 9.

Shan et al. (2022) showed that the DNN could provide excellent predictions of the ASCAT observables. Also, when averaged in time and across many GPIs (Shan et al., 2022), the NSCs were physically plausible and provided insight into the drivers of dynamics in the ASCAT observables. However, results in Fig. 9 here show that for a single GPI, at a single time step, the robustness and physical plausibility of the Jacobian may be limited. One key difference with respect to other studies is that we train a DNN for each GPI to account for mixing within the ASCAT footprint, rather than training a generic DNN per cover type. This reduces the amount of training data which, in turn, influences the robustness. Another potential difference is the complexity of the DNN, specifically the size of the input and output sets. Corchia et al. (2023) predict backscatter only, and account for the vegetation effects a priori by training the neural network with LAI from satellite observations. In contrast, we train the DNN to predict both backscatter and slope simultaneously and provide a large set of LSVs from the ISBA as input. These methodological differences may increase the complexity of the DNN, influencing the robustness of the Jacobians and hence the efficacy of assimilation. The third difference is the less direct relationship between the land surface model states and the observations, particularly

Table 3
Statistics of diagnostics of DA averaged across all GPIs, grassland GPIs and Agriculture GPIs.

	All GPIs		Grasslands		Agriculture	
	median	std	median	std	median	std
σ^o_{40} [dB]						
mean(innovations)	0.018	0.097	0.073	0.087	0.02	0.066
mean(residuals)	0.031	0.09	0.076	0.086	0.038	0.059
std(innovations)	0.29	0.092	0.23	0.048	0.39	0.077
std(residuals)	0.27	0.061	0.23	0.043	0.33	0.042
std(norm innovations)	0.83	0.18	0.68	0.13	1	0.12
mean$\lvert O-A/O-F\rvert$	0.92	0.07	0.98	0.026	0.86	0.07
C^k_{k+1} of innovations	0.37	0.067	0.33	0.054	0.36	0.086
$\sigma^{'}$ [dB/deg]						
mean(innovations)	0.00055	0.0011	0.00039	0.00078	0.00079	0.0012
mean(residuals)	0.00041	0.001	0.00035	0.00074	0.00065	0.0011
std(innovations)	0.0047	0.0014	0.0037	0.0009	0.0053	0.0013
std(residuals)	0.0041	0.0012	0.0035	0.0008	0.004	0.0015
std(norm innovations)	0.86	0.26	0.7	0.17	0.78	0.3
mean$\lvert O-A/O-F\rvert$	0.86	0.11	0.93	0.057	0.8	0.13
C^k_{k+1} of of innovations	0.81	0.17	0.89	0.11	0.64	0.21

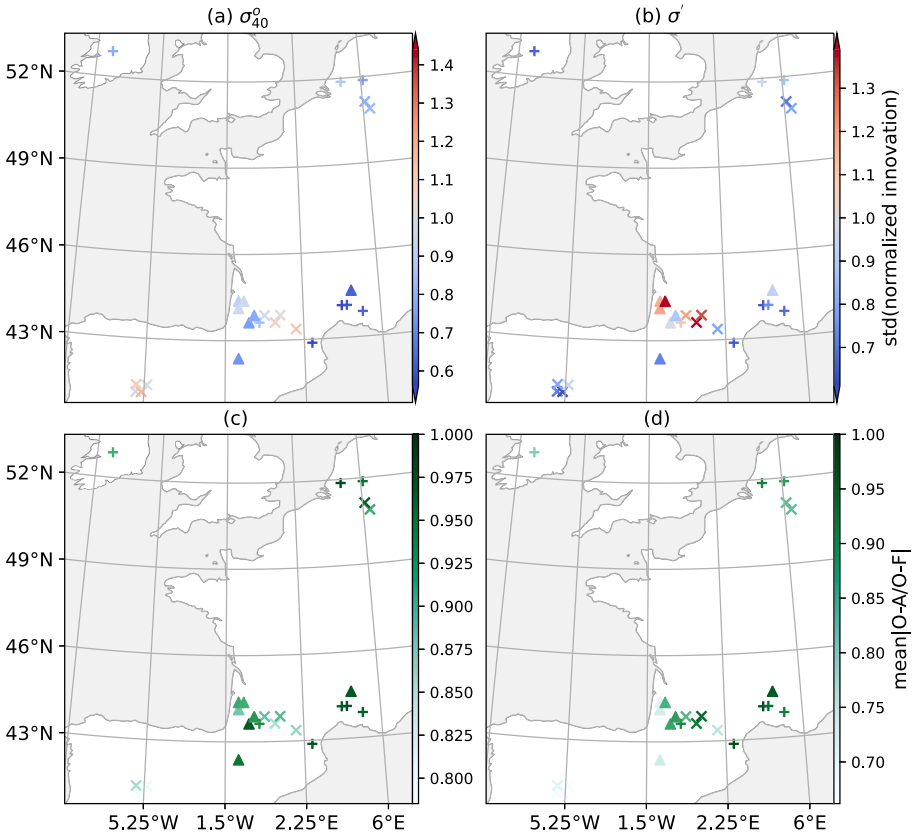

Fig. 6. Diagnostics of DA(σ^o_{40}, $\sigma^{'}$) from 2017 to 2019. Different rows show the standard deviation of normalized innovations and the time series mean values of $\lvert\frac{O-A}{O-F}\rvert$. Different rows show different observations (σ^o_{40} and $\sigma^{'}$). Agricultural GPIs are marked as 'x', grasslands GPIs as'+' and other GPIs as triangles.

between LSM states and ASCAT slope. While these indirect relationships are not problematic for predicting the observations, the absence of the expected improvement over the OL in our DA results suggests that they may be problematic in the DA framework. This study is therefore not a comparison of DA approaches. It is a study on the implications of including an observation operator based on machine learning in a DA framework. This is important due to the growing interest in using data-driven methods in data assimilation (Forman and Xue, 2016; Xue et al., 2018; Shamambo, 2020; de Roos et al., 2023; Corchia et al., 2023).

Results presented here suggest that successful use of ML-derived observation operators in assimilation hinges not just on good agreement between predicted and true observables, but also on the correct and robust estimation of the Jacobians. In cases like ours, where training data are limited, robustness of the Jacobian should be included as a criteria for selecting the optimal DNN (or other ML) model to map the LSVs to the observables. However, it is not trivial to achieve physical consistency in the sensitivities of the DNN to land surface variables. Future work is needed to examine the consistency of the DNN under

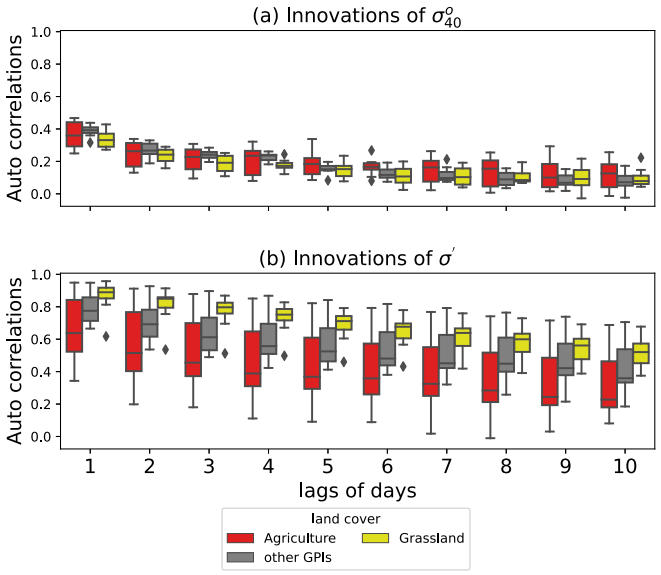

Fig. 7. Boxplots of autocorrelation of the innovations of (a) σ^o_{40} and (b) σ' at lags of different days. Agricultural GPIs are marked as red, grasslands GPIs as yellow and other GPIs as grey. The box extends from the lower to upper quartile values of the data, with a line at the median. The lower whisker is at the lowest datum above Q1–1.5*(Q3-Q1), and the upper whisker at the highest datum below Q3 + 1.5*(Q3-Q1), where Q1 and Q3 are the first and third quartiles. Outliers are indicated as grey dots. (For interpretation of the references to colour in this figure legend, the reader is referred to the web version of this article.)

different set of inputs and reduce the uncertainty of the DNN. Additionally, it is recommended to carefully quantify the observation error, particularly that of the slope, for future assimilation.

5. Conclusions

ASCAT normalized backscatter and slope were assimilated into the ISBA LSM to constrain soil water and vegetation dynamics. The ISBA LSM simulates surface fluxes of water, carbon and energy at the sub-grid (patch) level and aggregates the results to the grid scale. Here, ASCAT grid level observations were assimilated to produce the updated variables for grid points containing ISMN stations. Following Albergel et al. (2017), Barbu et al. (2014) and Barbu et al. (2011), SEKF was used as the DA algorithm. A DNN trained, tested and validated by Shan et al. (2022) was used as the observation operator linking model states with the ASCAT observations. The DA and OL were evaluated against ISMN in-situ station-based soil moisture observations and Copernicus LAI observations to test whether assimilating ASCAT observables helps to constrain the estimates of soil moisture and LAI. Results showed that, in general, the DA has a detrimental effect on the domain median values of ubRMSE and ρ of LAI and neutral effects on SSM (WG3) and RZSM (WG4&WG5). For deeper layers (WG6, WG7 and WG8), large updates are introduced by the assimilation. This is due to the large magnitudes of the Jacobians relating the ASCAT observables to soil moisture in deep layers.

Diagnostics were also analyzed to assess the Gaussianity of innovations and the optimality of the DA system, as well as the prescribed observation and model error. The time series mean of innovations of σ^o_{40} and σ' are within a reasonable range and are small, showing that our DA system reduces the uncertainties of the states in a long time period. The reduction in the standard deviation of residuals compared to the in-

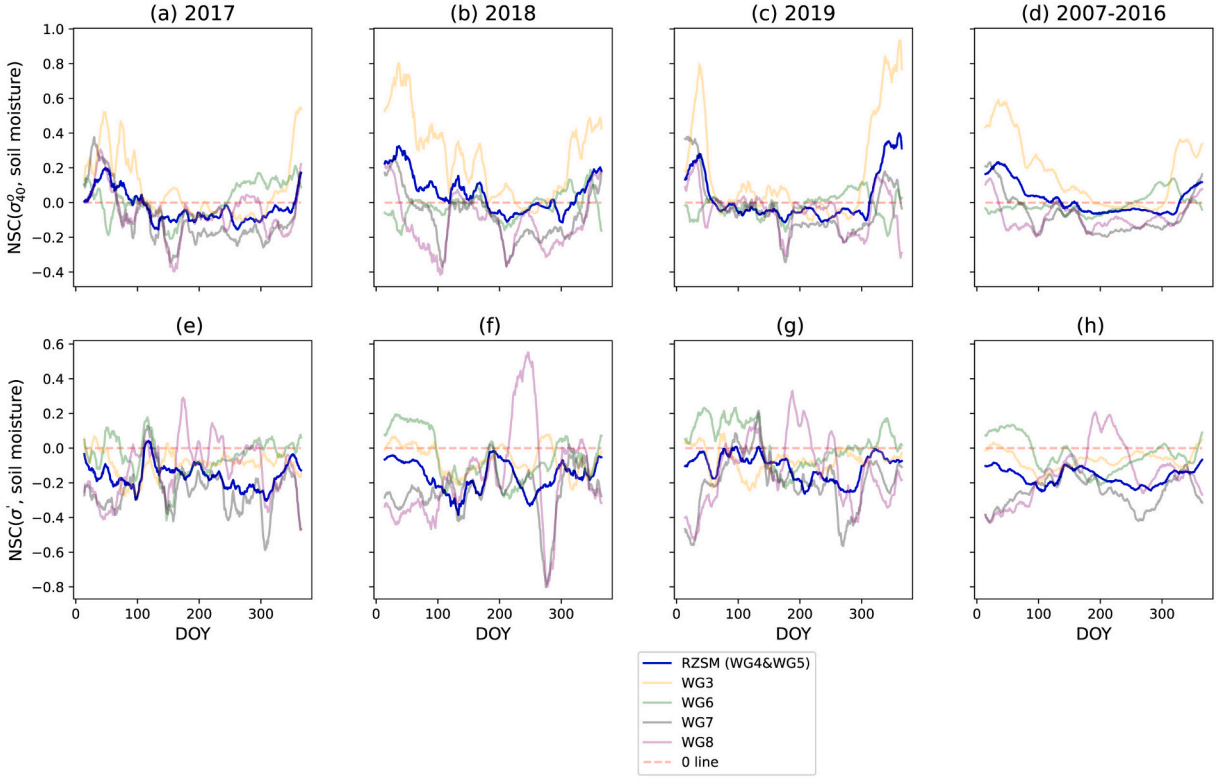

Fig. 8. Time series plot of NSC of ASCAT σ^o_{40} and σ' to soil moisture in each layers in independent validation years (2017, 2018 and 2019) and training years (2007–2016) averaged on agri GPIs containing ISMN stations: Saint Felix de Lauragais, Lahas, Condom and Savenes in SMOSMANIA network).

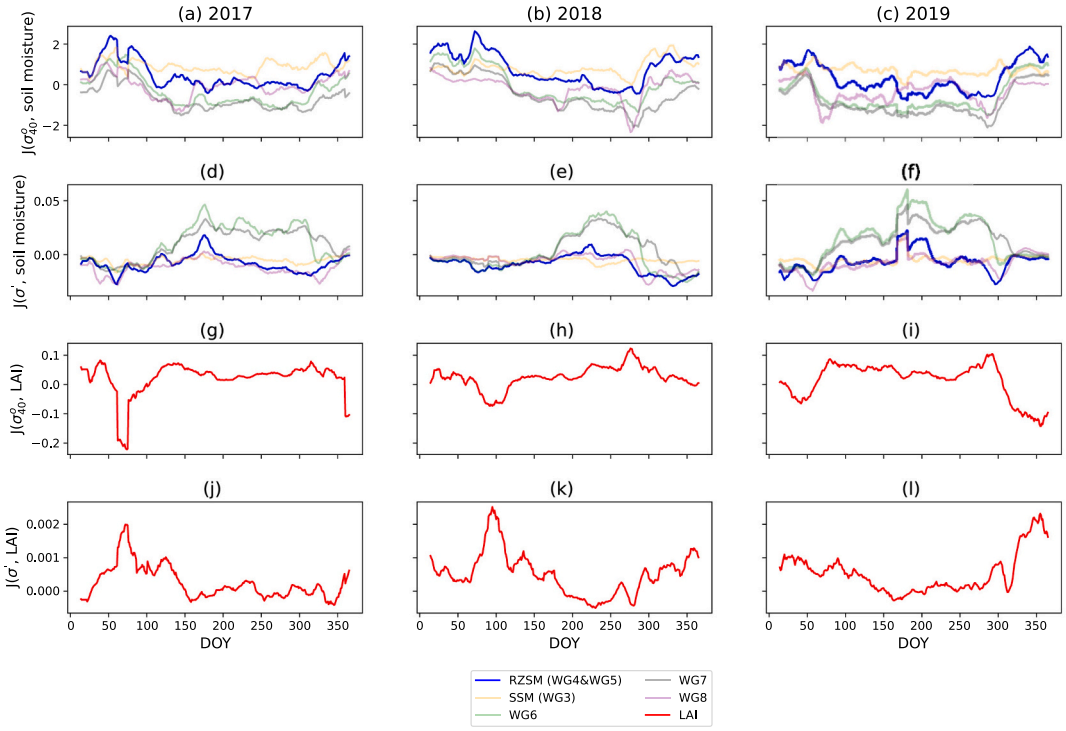

Fig. 9. Time series plot of aggregated J matrix in eq. (7) of ASCAT σ^o_{40} and $\acute{\sigma}$ to soil moisture in each layers in 2017, 2018 and 2019 averaged on agri GPIs containing ISMN stations: Saint Felix de Lauragais, Lahas, Condom and Savenes in SMOSMANIA network).

novations demonstrates the decrease in uncertainties following the assimilation of ASCAT σ^o_{40} and $\acute{\sigma}$ into the DA system. The analysis of normalized innovations and $|O-A/O-F|$ indicated that the model and observation errors are overestimated and this mis-specification is more problematic in grassland compared to agricultural areas. In other words, our prescribed observation error is more confident in agricultural GPIs. This could be related to the larger dynamic range of the ASCAT observables in agricultures GPIs shown in Fig. S1. Further, large values of lagged autocorrelation of the innovations indicate that the DA system is suboptimal and the information in ASCAT observables are not effectively used. Potential causes include the misspecification of the forecast and observation error, and the consistency of DNN sensitivities and predictions.

We investigated potential explanations for the limited positive impact of the DA. A second DA experiment was conducted with lower observation errors on agricultural GPIs. The comparison showed that the DA experiment with reduced observation errors does not perform better than the prescribed observation error, though the reduced observation errors reduces the suboptimality of the DA system. This indicated that the inconsistent sensitivities of the Deep Neural Network (DNN) used in the observation operator may have a greater influence on the updates than the model and observation errors themselves.

With the growing utilization of machine-learning-based observation operators in land data assimilation systems, this study underscores the importance of addressing the robustness of the machine learning (ML) methods. A key result of this study is that successful ML training does not ensure successful DA, as the terms of the Jacobian may include spurious effects due to overfitting if too many predictors (inputs) are used in the DNN. Therefore, the robustness of ML-based methods plays a vital role in ensuring the physical plausibility of land-atmosphere mechanisms learned by the data-driven approaches, particularly in terms of the sensitivities of remote sensing observables to land surface variables. Furthermore, this is essential to ensure transferability of machine learning algorithms as observation operators for assimilating similar remote sensing data into LSMs.

CRediT authorship contribution statement

Xu Shan: Writing – review & editing, Writing – original draft, Visualization, Validation, Methodology, Investigation, Formal analysis, Conceptualization. **Susan Steele-Dunne:** Writing – review & editing, Supervision, Resources, Project administration, Methodology, Investigation, Funding acquisition, Formal analysis, Conceptualization. **Sebastian Hahn:** Writing – review & editing, Resources. **Wolfgang Wagner:** Writing – review & editing, Resources. **Bertrand Bonan:** Writing – review & editing, Resources. **Clement Albergel:** Writing – review & editing, Resources. **Jean-Christophe Calvet:** Writing – review & editing, Resources. **Ou Ku:** Software.

Declaration of competing interest

The authors declare that they have no known competing financial interests or personal relationships that could have appeared to influence the work reported in this paper.

Data availability

I have shared the link to the data at the File Attach step
Dataset of ISBA open loop states and ASCAT normalized backscatter and slope data of grid points (Original data) (4TU)

Acknowledgement

X.S and S·S-D are supported by Dutch Research Foundation (NWO) - User Support Programme Space Research [grant number ALWGO.2018.036] with support from the Netherlands eScience Center [Grant number NLeSC C19.007]. Ths work was carried out on the Dutch national e-infrastructure with the support of SURF Cooperative. X.S and S·S-D were responsible for the conceptualization, methodology, formal analysis, investigation, visualization and writing (original draft

preparation). S.H. and W.W. provided resources (ASCAT data). B.B., C. A. and J-C.C. provided resources (ISBA model simulations). O.K. contributed to the methodology and investigation. All authors contributed to the analysis of results and writing (review and editing). The authors declare no conflict of interest. Data of ISBA open loop and ASCAT observables are available at https://data.4tu.nl/private_datasets/oCfGf2Lq1CNG8Qtrl2T-0ucNO4QweRHw7c1eNurE_u4.

Appendix A. Supplementary data

Supplementary data to this article can be found online at https://doi.org/10.1016/j.rse.2024.114167.

References

Aires, F., Weston, P., Rosnay, P., Fairbairn, D., 2021. Statistical approaches to assimilate ASCAT soil moisture information—i. methodologies and first assessment. Q. J. Roy. Meteorol. Soc. https://doi.org/10.1002/qj.3997.

Albergel, C., Rüdiger, C., Carrer, D., Calvet, J.C., Fritz, N., Naeimi, V., Bartalis, Z., Hasenauer, S., 2009. An evaluation of ASCAT surface soil moisture products with in-situ observations in southwestern France. Hydrol. Earth Syst. Sci. 13, 115–124. https://doi.org/10.5194/hess-13-115-2009.

Albergel, C., Calvet, J.C., Mahfouf, J.F., Rüdiger, C., Barbu, A.L., Lafont, S., Roujean, J.L., Walker, J.P., Crapeau, M., Wigneron, J.P., 2010. Monitoring of water and carbon fluxes using a land data assimilation system: a case study for southwestern France. Hydrol. Earth Syst. Sci. 14, 1109–1124. https://doi.org/10.5194/hess-14-1109-2010.

Albergel, C., de Rosnay, P., Gruhier, C., Muñoz-Sabater, J., Hasenauer, S., Isaksen, L., Kerr, Y., Wagner, W., 2012. Evaluation of remotely sensed and modelled soil moisture products using global ground-based in situ observations. Remote Sens. Environ. 118, 215–226. https://doi.org/10.1016/j.rse.2011.11.017.

Albergel, C., Munier, S., Leroux, D.J., Dewaele, H., Fairbairn, D., Barbu, A.L., Gelati, E., Dorigo, W., Faroux, S., Meurey, C., Moigne, P.L., Decharme, B., Mahfouf, J.F., Calvet, J.C., 2017. Sequential assimilation of satellite-derived vegetation and soil moisture products using SURFEX_v8.0: LDAS-monde assessment over the euro-mediterranean area. Geosci. Model Dev. 10, 3889–3912. https://doi.org/10.5194/gmd-10-3889-2017.

Albergel, C., Munier, S., Bocher, A., Bonan, B., Zheng, Y., Draper, C., Leroux, D., Calvet, J.C., 2018. LDAS-monde sequential assimilation of satellite derived observations applied to the contiguous US: an ERA-5 driven reanalysis of the land surface variables. Remote Sens. (Basel) 10, 1627. https://doi.org/10.3390/rs10101627.

Albergel, C., Dutra, E., Bonan, B., Zheng, Y., Munier, S., Balsamo, G., de Rosnay, P., Muñoz-Sabater, J., Calvet, J.C., 2019. Monitoring and forecasting the impact of the 2018 summer heatwave on vegetation. Remote Sens. (Basel) 11, 520. https://doi.org/10.3390/rs11050520.

Albergel, C., Zheng, Y., Bonan, B., Dutra, E., Rodríguez-Fernández, N., Munier, S., Draper, C., de Rosnay, P., Muñoz-Sabater, J., Balsamo, G., Fairbairn, D., Meurey, C., Calvet, J.C., 2020. Data assimilation for continuous global assessment of severe conditions over terrestrial surfaces. Hydrol. Earth Syst. Sci. 24, 4291–4316. https://doi.org/10.5194/hess-24-4291-2020.

Attema, E.P.W., Ulaby, F.T., 1978. Vegetation modeled as a water cloud. Radio Sci. 13, 357–364. https://doi.org/10.1029/rs013i002p00357.

Baguis, P., Carrassi, A., Roulin, E., Vannitsem, S., Modanesi, S., Lievens, H., Bechtold, M., Lannoy, G.D., 2022. Assimilation of backscatter observations into a hydrological model: a case study in Belgium using ASCAT data. Remote Sens. (Basel) 14, 5740. https://doi.org/10.3390/rs14225740.

Balsamo, G., Mahfouf, J.F., Bélair, S., Deblonde, G., 2006. A global root-zone soil moisture analysis using simulated l-band brightness temperature in preparation for the hydros satellite mission. J. Hydrometeorol. 7, 1126–1146. https://doi.org/10.1175/jhm525.1.

Barbu, A., Calvet, J.C., Mahfouf, J.F., Albergel, C., Lafont, S., 2011. Assimilation of soil wetness index and leaf area index into the isba-a-gs land surface model: grassland case study. Biogeosciences 8, 1971–1986.

Barbu, A.L., Calvet, J.C., Mahfouf, J.F., Lafont, S., 2014. Integrating ASCAT Surface Soil Moisture and GEOV1 Leaf Area Index into the SURFEX Modelling Platform: A Land Data Assimilation Application over France, 18, pp. 173–192. https://doi.org/10.5194/hess-18-173-2014.

Bartalis, Z., Wagner, W., Naeimi, V., Hasenauer, S., Scipal, K., Bonekamp, H., Figa, J., Anderson, C., 2007. Initial soil moisture retrievals from the METOP-a advanced scatterometer (ASCAT). Geophys. Res. Lett. 34 https://doi.org/10.1029/2007gl031088.

Berg, A., Findell, K., Lintner, B., Giannini, A., Seneviratne, S.I., van den Hurk, B., Lorenz, R., Pitman, A., Hagemann, S., Meier, A., Cheruy, F., Ducharne, A., Malyshev, S., Milly, P.C.D., 2016. Land–atmosphere feedbacks amplify aridity increase over land under global warming. Nature. Climate Change 6, 869–874. https://doi.org/10.1038/nclimate3029.

Bonan, B., Albergel, C., Zheng, Y., Barbu, A.L., Fairbairn, D., Munier, S., Calvet, J.C., 2020. An ensemble square root filter for the joint assimilation of surface soil moisture and leaf area index within the land data assimilation system LDAS-monde: application over the euro-mediterranean region. Hydrol. Earth Syst. Sci. 24, 325–347. https://doi.org/10.5194/hess-24-325-2020.

Brocca, L., Melone, F., Moramarco, T., Wagner, W., Naeimi, V., Bartalis, Z., Hasenauer, S., 2010. Improving runoff prediction through the assimilation of the ASCAT soil moisture product. Hydrol. Earth Syst. Sci. 14, 1881–1893. https://doi.org/10.5194/hess-14-1881-2010.

Calvet, J.C., Noilhan, J., Roujean, J.L., Bessemoulin, P., Cabelguenne, M., Olioso, A., Wigneron, J.P., 1998. An interactive vegetation SVAT model tested against data from six contrasting sites. Agric. For. Meteorol. 92, 73–95. https://doi.org/10.1016/s0168-1923(98)00091-4.

Calvet, J.C., Rivalland, V., Picon-Cochard, C., Guehl, J.M., 2004. Modelling forest transpiration and CO2 fluxes—response to soil moisture stress. Agric. For. Meteorol. 124, 143–156. https://doi.org/10.1016/j.agrformet.2004.01.007.

Calvet, J.C., Fritz, N., Froissard, F., Suquia, D., Petitpa, A., Piguet, B., 2007. In situ soil moisture observations for the CAL/VAL of SMOS: the SMOSMANIA network. In: 2007 IEEE International Geoscience and Remote Sensing Symposium. IEEE. https://doi.org/10.1109/igarss.2007.4423019.

Corchia, T., Bonan, B., Rodríguez-Fernández, N., Colas, G., Calvet, J.C., 2023. Assimilation of ASCAT radar backscatter coefficients over southwestern France. Remote Sens. (Basel) 15, 4258. https://doi.org/10.3390/rs15174258.

Crow, W.T., Wood, E.F., 2003. The assimilation of remotely sensed soil brightness temperature imagery into a land surface model using ensemble kalman filtering: a case study based on ESTAR measurements during SGP97. Adv. Water Resour. 26, 137–149. https://doi.org/10.1016/s0309-1708(02)00088-x.

Daley, R., 1992. The lagged innovation covariance: a performance diagnostic for atmospheric data assimilation. Monthly weather review 120, 178–196. https://doi.org/10.1175/1520-0493(1992)120<0178:tlicap>2.0.co;2.

de Roos, S., Busschaert, L., Lievens, H., Bechtold, M., Lannoy, G.J.D., 2023. Optimisation of AquaCrop backscatter simulations using sentinel-1 observations. Remote Sens. Environ. 294, 113621. https://doi.org/10.1016/j.rse.2023.113621.

Dee, D.P., 2005. Bias and data assimilation. Q. J. Roy. Meteorol. Soc. 131, 3323–3343. https://doi.org/10.1256/qj.05.137.

Desroziers, G., Berre, L., Chapnik, B., Poli, P., 2005. Diagnosis of observation, background and analysis-error statistics in observation space. Q. J. Roy. Meteorol. Soc. 131, 3385–3396. https://doi.org/10.1256/qj.05.108.

Dorigo, W.A., Wagner, W., Hohensinn, R., Hahn, S., Paulik, C., Xaver, A., Gruber, A., Drusch, M., Mecklenburg, S., van Oevelen, P., Robock, A., Jackson, T., 2011. The international soil moisture network: a data hosting facility for global in situ soil moisture measurements. Hydrol. Earth Syst. Sci. 15, 1675–1698. https://doi.org/10.5194/hess-15-1675-2011.

Dorigo, W., Xaver, A., Vreugdenhil, M., Gruber, A., Hegyiová, A., Sanchis-Dufau, A., Zamojski, D., Cordes, C., Wagner, W., Drusch, M., 2013. Global automated quality control of in situ soil moisture data from the international soil moisture network. Vadose Zone J. 12 https://doi.org/10.2136/vzj2012.0097 vzj2012.0097.

Draper, C.S., Walker, J.P., Steinle, P.J., de Jeu, R.A., Holmes, T.R., 2009. An evaluation of AMSR–e derived soil moisture over Australia. Remote Sens. Environ. 113, 703–710. https://doi.org/10.1016/j.rse.2008.11.011.

Draper, C., Mahfouf, J.F., Calvet, J.C., Martin, E., Wagner, W., 2011. Assimilation of ASCAT near-surface soil moisture into the SIM hydrological model over France. Hydrol. Earth Syst. Sci. 15, 3829–3841. https://doi.org/10.5194/hess-15-3829-2011.

Draper, C.S., Reichle, R.H., Lannoy, G.J.M.D., Liu, Q., 2012. Assimilation of passive and active microwave soil moisture retrievals. Geophys. Res. Lett. 39 https://doi.org/10.1029/2011gl050655 n/a–n/a.

Entekhabi, D., Njoku, E.G., O'Neill, P.E., Kellogg, K.H., Crow, W.T., Edelstein, W.N., Entin, J.K., Goodman, S.D., Jackson, T.J., Johnson, J., Kimball, J., Piepmeier, J.R., Koster, R.D., Martin, N., McDonald, K.C., Moghaddam, M., Moran, S., Reichle, R., Shi, J.C., Spencer, M.W., Thurman, S.W., Tsang, L., Zyl, J.V., 2010. The soil moisture active passive (SMAP) mission. Proc. IEEE 98, 704–716. https://doi.org/10.1109/jproc.2010.2043918.

Entekhabi, D., Yueh, S., O'Neill, P.E., Kellogg, K.H., Allen, A., Bindlish, R., Brown, M., Chan, S., Colliander, A., Crow, W.T., et al., 2014. Smap Handbook–Soil Moisture Active Passive: Mapping Soil Moisture and Freeze/Thaw from Space.

Fairbairn, D., Barbu, A.L., Napoly, A., Albergel, C., Mahfouf, J.F., Calvet, J.C., 2017. The effect of satellite-derived surface soil moisture and leaf area index land data assimilation on streamflow simulations over France. Hydrol. Earth Syst. Sci. 21, 2015–2033. https://doi.org/10.5194/hess-21-2015-2017.

Forman, B.A., Reichle, R.H., 2015. Using a support vector machine and a land surface model to estimate large-scale passive microwave brightness temperatures over snow-covered land in north america. IEEE Journal of Selected Topics in Applied Earth Observations and Remote Sensing 8, 4431–4441. https://doi.org/10.1109/jstars.2014.2325780.

Forman, B.A., Xue, Y., 2016. Machine learning predictions of passive microwave brightness temperature over snow-covered land using the special sensor microwave imager (SSM/I). Phys. Geogr. 38, 176–196. https://doi.org/10.1080/02723646.2016.1236606.

Gruber, A., Lannoy, G.D., Albergel, C., Al-Yaari, A., Brocca, L., Calvet, J.C., Colliander, A., Cosh, M., Crow, W., Dorigo, W., Draper, C., Hirschi, M., Kerr, Y., Konings, A., Lahoz, W., McColl, K., Montzka, C., Muñoz-Sabater, J., Peng, J., Reichle, R., Richaume, P., Rüdiger, C., Scanlon, T., van der Schalie, R., Wigneron, J. P., Wagner, W., 2020. Validation practices for satellite soil moisture retrievals: what are (the) errors? Remote Sens. Environ. 244, 111806. https://doi.org/10.1016/j.rse.2020.111806.

Hahn, S., Reimer, C., Vreugdenhil, M., Melzer, T., Wagner, W., 2017. Dynamic characterization of the incidence angle dependence of backscatter using metop ASCAT. E 10, 2348–2359. https://doi.org/10.1109/jstars.2016.2628523.

Han, X., Franssen, H.J.H., Montzka, C., Vereecken, H., 2014. Soil moisture and soil properties estimation in the community land model with synthetic brightness temperature observations. Water Resour. Res. 50, 6081–6105. https://doi.org/10.1002/2013wr014586.

Hersbach, H., Bell, B., Berrisford, P., Hirahara, S., Horányi, A., Muñoz-Sabater, J., Nicolas, J., Peubey, C., Radu, R., Schepers, D., Simmons, A., Soci, C., Abdalla, S., Abellan, X., Balsamo, G., Bechtold, P., Biavati, G., Bidlot, J., Bonavita, M., Chiara, G., Dahlgren, P., Dee, D., Diamantakis, M., Dragani, R., Flemming, J., Forbes, R., Fuentes, M., Geer, A., Haimberger, L., Healy, S., Hogan, R.J., Hólm, E., Janisková, M., Keeley, S., Laloyaux, P., Lopez, P., Lupu, C., Radnoti, G., Rosnay, P., Rozum, I., Vamborg, F., Villaume, S., Thépaut, J.N., 2020. The ERA5 global reanalysis. Q. J. Roy. Meteorol. Soc. 146, 1999–2049. https://doi.org/10.1002/qj.3803.

Imaoka, K., Kachi, M., Kasahara, M., Ito, N., Nakagawa, K., Oki, T., 2010. Instrument performance and calibration of amsr-e and amsr2. International archives of the photogrammetry, remote sensing and spatial information science, 38, pp. 13–18.

Jacobs, C., van den Hurk, B., de Bruin, H., 1996. Stomatal behaviour and photosynthetic rate of unstressed grapevines in semi-arid conditions. Agric. For. Meteorol. 80, 111–134. https://doi.org/10.1016/0168-1923(95)02295-3.

Kailath, T., 1968. An innovations approach to least-squares estimation–part i: linear filtering in additive white noise. IEEE Trans Automat Contr 13, 646–655. https://doi.org/10.1109/tac.1968.1099025.

Kerr, Y.H., Waldteufel, P., Wigneron, J.P., Delwart, S., Cabot, F., Boutin, J., Escorihuela, M.J., Font, J., Reul, N., Gruhier, C., Juglea, S.E., Drinkwater, M.R., Hahne, A., Martín-Neira, M., Mecklenburg, S., 2010. The SMOS mission: new tool for monitoring key elements ofthe global water cycle. Proc. IEEE 98, 666–687. https://doi.org/10.1109/jproc.2010.2043032.

Kolassa, J., Reichle, R., Draper, C., 2017. Merging active and passive microwave observations in soil moisture data assimilation. Remote Sens. Environ. 191, 117–130. https://doi.org/10.1016/j.rse.2017.01.015.

Koster, R.D., Chang, Y., Wang, H., Schubert, S.D., 2016. Impacts of local soil moisture anomalies on the atmospheric circulation and on remote surface meteorological fields during boreal summer: a comprehensive analysis over north america. J. Climate 29, 7345–7364. https://doi.org/10.1175/jcli-d-16-0192.1.

Kumar, S.V., Holmes, T.R., Bindlish, R., de Jeu, R., Peters-Lidard, C., 2020. Assimilation of vegetation optical depth retrievals from passive microwave radiometry. Hydrol. Earth Syst. Sci. 24, 3431–3450. https://doi.org/10.5194/hess-24-3431-2020.

Lannoy, G.J.M.D., Reichle, R.H., 2016a. Assimilation of SMOS brightness temperatures or soil moisture retrievals into a land surface model. Hydrol. Earth Syst. Sci. 20, 4895–4911. https://doi.org/10.5194/hess-20-4895-2016.

Lannoy, G.J.M.D., Reichle, R.H., 2016b. Global assimilation of multiangle and multipolarization SMOS brightness temperature observations into the GEOS-5 catchment land surface model for soil moisture estimation. J. Hydrometeorol. 17, 669–691. https://doi.org/10.1175/jhm-d-15-0037.1.

Leroux, D., Calvet, J.C., Munier, S., Albergel, C., 2018. Using satellite-derived vegetation products to evaluate LDAS-monde over the euro-mediterranean area. Remote Sens. (Basel) 10, 1199. https://doi.org/10.3390/rs10081199.

Lievens, H., Tomer, S., Bitar, A.A., Lannoy, G.D., Drusch, M., Dumedah, G., Franssen, H.J. H., Kerr, Y., Martens, B., Pan, M., Roundy, J., Vereecken, H., Walker, J., Wood, E., Verhoest, N., Pauwels, V., 2015. SMOS soil moisture assimilation for improved hydrologic simulation in the Murray darling basin, Australia. Remote Sens. Environ. 168, 146–162. https://doi.org/10.1016/j.rse.2015.06.025.

Lievens, H., Martens, B., Verhoest, N., Hahn, S., Reichle, R., Miralles, D., 2017a. Assimilation of global radar backscatter and radiometer brightness temperature observations to improve soil moisture and land evaporation estimates. Remote Sens. Environ. 189, 194–210. https://doi.org/10.1016/j.rse.2016.11.022.

Lievens, H., Reichle, R.H., Liu, Q., Lannoy, G.J.M.D., Dunbar, R.S., Kim, S.B., Das, N.N., Cosh, M., Walker, J.P., Wagner, W., 2017b. Joint sentinel-1 and SMAP data assimilation to improve soil moisture estimates. Geophys. Res. Lett. 44, 6145–6153. https://doi.org/10.1002/2017gl073904.

Lu, Y., Steele-Dunne, S.C., Lannoy, G.J.M.D., 2020. Improving soil moisture and surface turbulent heat flux estimates by assimilation of SMAP brightness temperatures or soil moisture retrievals and GOES land surface temperature retrievals. J. Hydrometeorol. 21, 183–203. https://doi.org/10.1175/jhm-d-19-0130.1.

Mahfouf, J.F., Bergaoui, K., Draper, C., Bouyssel, F., Taillefer, F., Taseva, L., 2009. A comparison of two off-line soil analysis schemes for assimilation of screen level observations. J. Geophys. Res. 114 https://doi.org/10.1029/2008jd011077.

Martens, B., Miralles, D., Lievens, H., Fernández-Prieto, D., Verhoest, N., 2016. Improving terrestrial evaporation estimates over continental Australia through assimilation of SMOS soil moisture. Int. J. Appl. Earth Obs. Geoinf. 48, 146–162. https://doi.org/10.1016/j.jag.2015.09.012.

Masson, V., Moigne, P.L., Martin, E., Faroux, S., Alias, A., Alkama, R., Belamari, S., Barbu, A., Boone, A., Bouyssel, F., Brousseau, P., Brun, E., Calvet, J.C., Carrer, D., Decharme, B., Delire, C., Donier, S., Essaouini, K., Gibelin, A.L., Giordani, H., Habets, F., Jidane, M., Kerdraon, G., Kourzeneva, E., Lafaysse, M., Lafont, S., Brossier, C.L., Lemonsu, A., Mahfouf, J.F., Marguinaud, P., Mokhtari, M., Morin, S., Pigeon, G., Salgado, R., Seity, Y., Taillefer, F., Tanguy, G., Tulet, P., Vincendon, B., Vionnet, V., Voldoire, A., 2013. The SURFEXv7.2 land and ocean surface platform for coupled or offline simulation of earth surface variables and fluxes. Geosci. Model Dev. 6, 929–960. https://doi.org/10.5194/gmd-6-929-2013.

Mecklenburg, S., Drusch, M., Kaleschke, L., Rodriguez-Fernandez, N., Reul, N., Kerr, Y., Font, J., Martin-Neira, M., Oliva, R., Daganzo-Eusebio, E., Grant, J., Sabia, R., Macelloni, G., Rautiainen, K., Fauste, J., de Rosnay, P., Munoz-Sabater, J., Verhoest, N., Lievens, H., Delwart, S., Crapolicchio, R., de la Fuente, A., Kornberg, M., 2016. ESA's soil moisture and ocean salinity mission: from science to operational applications. Remote Sens. Environ. 180, 3–18. https://doi.org/10.1016/j.rse.2015.12.025.

Melzer, T., 2013. Vegetation modelling in warp 6.0. In: Proceedings of the EUMETSAT Meteorological Satellite Conference, Vienna, Austria, pp. 16–20.

Miralles, D.G., Teuling, A.J., van Heerwaarden, C.C., de Arellano, J.V.G., 2014. Mega-heatwave temperatures due to combined soil desiccation and atmospheric heat accumulation. Nat. Geosci. 7, 345–349. https://doi.org/10.1038/ngeo2141.

Mladenova, I.E., Bolten, J.D., Crow, W., Sazib, N., Reynolds, C., 2020. Agricultural drought monitoring via the assimilation of SMAP soil moisture retrievals into a global soil water balance model. Frontiers in Big Data 3. https://doi.org/10.3389/fdata.2020.00010.

Modanesi, S., Massari, C., Bechtold, M., Lievens, H., Tarpanelli, A., Brocca, L., Zappa, L., Lannoy, G.J.M.D., 2022. Challenges and benefits of quantifying irrigation through the assimilation of sentinel-1 backscatter observations into noah-MP. Hydrol. Earth Syst. Sci. 26, 4685–4706. https://doi.org/10.5194/hess-26-4685-2022.

Mucia, A., Bonan, B., Albergel, C., Zheng, Y., Calvet, J.C., 2022. Assimilation of passive microwave vegetation optical depth in ldas-monde: a case study over the continental Usa. Biogeosciences 19, 2557–2581. https://doi.org/10.5194/bg-19-2557-2022.

Njoku, E., Jackson, T., Lakshmi, V., Chan, T., Nghiem, S., 2003. Soil moisture retrieval from AMSR-e. IEEE Trans. Geosci. Remote Sens. 41, 215–229. https://doi.org/10.1109/tgrs.2002.808243.

Noilhan, J., Mahfouf, J.F., 1996. The ISBA land surface parameterisation scheme. Global Planet. Change 13, 145–159. https://doi.org/10.1016/0921-8181(95)00043-7.

Noilhan, J., Planton, S., 1989. A simple parameterization of land surface processes for meteorological models. Mon. Weather Rev. 117, 536–549. https://doi.org/10.1175/1520-0493(1989)117<0536:aspols>2.0.co;2.

Petchiappan, A., Steele-Dunne, S.C., Vreugdenhil, M., Hahn, S., Wagner, W., Oliveira, R., 2021. The influence of vegetation water dynamics on the ASCAT backscatter-incidence angle relationship in the amazon. https://doi.org/10.5194/hess-2021-406.

Pfeil, I., Wagner, W., Forkel, M., Dorigo, W., Vreugdenhil, M., 2020. Does ASCAT observe the spring reactivation in temperate deciduous broadleaf forests? Remote Sens. Environ. 250, 112042 https://doi.org/10.1016/j.rse.2020.112042.

Pinnington, E., Amezcua, J., Cooper, E., Dadson, S., Ellis, R., Peng, J., Robinson, E., Morrison, R., Osborne, S., Quaife, T., 2021. Improving soil moisture prediction of a high-resolution land surface model by parameterising pedotransfer functions through assimilation of SMAP satellite data. Hydrol. Earth Syst. Sci. 25, 1617–1641. https://doi.org/10.5194/hess-25-1617-2021.

Rains, D., Lievens, H., Lannoy, G.J.M.D., Mccabe, M.F., de Jeu, R.A.M., Miralles, D.G., 2022. Sentinel-1 backscatter assimilation using support vector regression or the water cloud model at european soil moisture sites. IEEE Geosci. Remote Sens. Lett. 19, 1–5. https://doi.org/10.1109/lgrs.2021.3073484.

Reichle, R.H., Koster, R.D., 2004. Bias reduction in short records of satellite soil moisture. Geophys. Res. Lett. 31 https://doi.org/10.1029/2004gl020938.

Reichle, R.H., McLaughlin, D.B., Entekhabi, D., 2002a. Hydrologic data assimilation with the ensemble kalman filter. Monthly weather review 130, 103–114. https://doi.org/10.1175/1520-0493(2002)130<0103:hdawte>2.0.co;2.

Reichle, R.H., Walker, J.P., Koster, R.D., Houser, P.R., 2002b. Extended versus ensemble kalman filtering for land data assimilation. J. Hydrometeorol. 3, 728–740. https://doi.org/10.1175/1525-7541(2002)003<0728:evekff>2.0.co;2.

Reichle, R.H., Koster, R.D., Dong, J., Berg, A.A., 2004. Global soil moisture from satellite observations, land surface models, and ground data: implications for data assimilation. Journal of hydrometeorology 5, 430–442. https://doi.org/10.1175/1525-7541(2004)005<0430:gsmfso>2.0.co;2.

Reichle, R.H., Koster, R.D., Liu, P., Mahanama, S.P.P., Njoku, E.G., Owe, M., 2007. Comparison and assimilation of global soil moisture retrievals from the advanced microwave scanning radiometer for the earth observing system (AMSR-e) and the scanning multichannel microwave radiometer (SMMR). J. Geophys. Res. 112 https://doi.org/10.1029/2006jd008033.

Reichle, R.H., Lannoy, G.J.M.D., Liu, Q., Ardizzone, J.V., Colliander, A., Conaty, A., Crow, W., Jackson, T.J., Jones, L.A., Kimball, J.S., Koster, R.D., Mahanama, S.P., Smith, E.B., Berg, A., Bircher, S., Bosch, D., Caldwell, T.G., Cosh, M., González-Zamora, Á., Collins, C.D.H., Jensen, K.H., Livingston, S., Lopez-Baeza, E., Martínez-Fernández, J., McNairn, H., Moghaddam, M., Pacheco, A., Pellarin, T., Prueger, J., Rowlandson, T., Seyfried, M., Starks, P., Su, Z., Thibeault, M., van der Velde, R., Walker, J., Wu, X., Zeng, Y., 2017a. Assessment of the SMAP level-4 surface and root-zone soil moisture product using in situ measurements. J. Hydrometeorol. 18, 2621–2645. https://doi.org/10.1175/jhm-d-17-0063.1.

Reichle, R.H., Lannoy, G.J.M.D., Liu, Q., Koster, R.D., Kimball, J.S., Crow, W.T., Ardizzone, J.V., Chakraborty, P., Collins, D.W., Conaty, A.L., Girotto, M., Jones, L.A., Kolassa, J., Lievens, H., Lucchesi, R.A., Smith, E.B., 2017b. Global assessment of the SMAP level-4 surface and root-zone soil moisture product using assimilation diagnostics. J. Hydrometeorol. 18, 3217–3237. https://doi.org/10.1175/jhm-d-17-0130.1.

Reichle, R.H., Zhang, S.Q., Liu, Q., Draper, C.S., Kolassa, J., Todling, R., 2021. Assimilation of SMAP brightness temperature observations in the GEOS land–atmosphere data assimilation system. IEEE Journal of Selected Topics in Applied Earth Observations and Remote Sensing 14, 10628–10643. https://doi.org/10.1109/jstars.2021.3118595.

Ridler, M.E., Madsen, H., Stisen, S., Bircher, S., Fensholt, R., 2014. Assimilation of SMOS-derived soil moisture in a fully integrated hydrological and soil-vegetation-atmosphere transfer model in western Denmark. Water Resour. Res. 50, 8962–8981. https://doi.org/10.1002/2014wr015392.

Sabater, J.M., Jarlan, L., Calvet, J.C., Bouyssel, F., Rosnay, P.D., 2007. From near-surface to root-zone soil moisture using different assimilation techniques. J. Hydrometeorol. 8, 194–206. https://doi.org/10.1175/jhm571.1.

Sabater, J.M., Rüdiger, C., Calvet, J.C., Fritz, N., Jarlan, L., Kerr, Y., 2008. Joint assimilation of surface soil moisture and LAI observations into a land surface model. Agric. For. Meteorol. 148, 1362–1373. https://doi.org/10.1016/j.agrformet.2008.04.003.

Seo, E., Lee, M.I., Reichle, R.H., 2021. Assimilation of SMAP and ASCAT soil moisture retrievals into the JULES land surface model using the local ensemble transform kalman filter. Remote Sens. Environ. 253, 112222. https://doi.org/10.1016/j.rse.2020.112222.

Shamambo, D.C., 2020. Assimilation de données satellitaires pour le suivi des ressources en eau dans la zone Euro-Méditerranée. Ph.D. thesis. Toulouse 3.

Shan, X., Steele-Dunne, S., Huber, M., Hahn, S., Wagner, W., Bonan, B., Albergel, C., Calvet, J.C., Ku, O., Georgievska, S., 2022. Towards constraining soil and vegetation dynamics in land surface models: modeling ASCAT backscatter incidence-angle dependence with a deep neural network. Remote Sens. Environ. 279, 113116. https://doi.org/10.1016/j.rse.2022.113116.

Snoek, J., Larochelle, H., Adams, R.P., 2012. Practical bayesian optimization of machine learning algorithms. Adv. Neural Inf. Proces. Syst. 2951–2959.

Steele-Dunne, S.C., Friesen, J., van de Giesen, N., 2012. Using diurnal variation in backscatter to detect vegetation water stress. IEEE Trans. Geosci. Remote Sens. 50, 2618–2629. https://doi.org/10.1109/tgrs.2012.2194156.

Steele-Dunne, S.C., Hahn, S., Wagner, W., Vreugdenhil, M., 2019. Investigating vegetation water dynamics and drought using metop ASCAT over the north american grasslands. Remote Sens. Environ. 224, 219–235. https://doi.org/10.1016/j.rse.2019.01.004.

Verger, A., Baret, F., Weiss, M., 2014. Near real-time vegetation monitoring at global scale. IEEE Journal of Selected Topics in Applied Earth Observations and Remote Sensing 7, 3473–3481. https://doi.org/10.1109/jstars.2014.2328632.

Wagner, W., Lemoine, G., Borgeaud, M., Rott, H., 1999a. A study of vegetation cover effects on ERS scatterometer data. IEEE Trans. Geosci. Remote Sens. 37, 938–948. https://doi.org/10.1109/36.752212.

Wagner, W., Lemoine, G., Rott, H., 1999b. A method for estimating soil moisture from ERS scatterometer and soil data. Remote Sens. Environ. 70, 191–207. https://doi.org/10.1016/s0034-4257(99)00036-x.

Wagner, W., Lindorfer, R., Melzer, T., Hahn, S., Bauer-Marschallinger, B., Morrison, K., Calvet, J.C., Hobbs, S., Quast, R., Greimeister-Pfeil, I., Vreugdenhil, M., 2022. Widespread occurrence of anomalous c-band backscatter signals in arid environments caused by subsurface scattering. Remote Sens. Environ. 276, 113025. https://doi.org/10.1016/j.rse.2022.113025.

Wigneron, J.P., Kerr, Y., Waldteufel, P., Saleh, K., Escorihuela, M.J., Richaume, P., Ferrazzoli, P., de Rosnay, P., Gurney, R., Calvet, J.C., Grant, J., Guglielmetti, M., Hornbuckle, B., Mätzler, C., Pellarin, T., Schwank, M., 2007. L-band microwave emission of the biosphere (l-MEB) model: description and calibration against experimental data sets over crop fields. Remote Sens. Environ. 107, 639–655. https://doi.org/10.1016/j.rse.2006.10.014.

Xue, Y., Forman, B.A., 2015. Comparison of passive microwave brightness temperature prediction sensitivities over snow-covered land in north america using machine learning algorithms and the advanced microwave scanning radiometer. Remote Sens. Environ. 170, 153–165. https://doi.org/10.1016/j.rse.2015.09.009.

Xue, Y., Forman, B.A., Reichle, R.H., 2018. Estimating snow mass in north america through assimilation of advanced microwave scanning radiometer brightness temperature observations using the catchment land surface model and support vector machines. Water Resour. Res. 54, 6488–6509. https://doi.org/10.1029/2017wr022219.